Modeling of Gamma-Ray Glows from Thunderclouds with GEANT4

Master Thesis in Space Physics

by

Ragnar D Landet

Dissertation for the degree of Master Of Science (MSc)
at the University of Bergen

2021

Scientific environment

This study is carried out at the Department of Physics and Technology, University of Bergen. The work is supported by the Birkeland Centre For Space Science.

Acknowledgements

This project has been a journey in discovery of the joy of scientific research for the writer. The experience had not been possible without the support and guidance of the staff at Birkeland centre for space science (BCSS) in Bergen. I would therefore take the opportunity to direct thanks to those that have been involved in shaping the result and the experience.

Thanks are directed to my supervisor, Nikolai Østgaard. His interest in the project and demand for high quality has been the major driver behind the project. The high standards that are demanded shaped the writer in delivering the needed results. I am truly grateful for all the help awarded by the co-supervisor, David Sarria, David is always helpful and he knows how to explain coding and physics to the students in a way that makes us understand.

Ragnar D Landet
Bergen, November 22, 2021

Abstract

Observations of high-energy x-ray radiation from thunderstorms began in the 1980s with airplane flights and later with balloons in the 1990s. The observations were conducted in search of evidence to support the predictions made by *Wilson* (1925), that runaway electrons could be responsible for x-ray radiation from thunderclouds. Later it has been known that there exists different forms of x-ray radiation in conjunction with thunderstorms, the highest radiation levels coming from Terrestrial Gamma-ray Flashes (TGF) and lower levels with longer timescales from gamma-ray glows. To explain the x-ray radiation two different production theories have been developed in the scientific community, the RREA process and the MOS process.

The purpose of this thesis is to build a simulation tool in Geometry and tracking 4 (GEANT4) to study the production mechanisms behind gamma-ray glows. The work has been focused on utilizing cosmic ray particles as seeds for x-ray radiation production in thundercloud electric fields. To create this tool an initial particle distribution is collected from the PHITS-based Analytical Radiation Model in the Atmosphere (PARMA) database. The PARMA database is based on Monte Carlo (MC) simulations and its data has been compared to experimental data [*Sato* (2016)].

To check the feasibility of the method particles has been propagated between different altitudes and results have been compared to the PARMA database. The purpose being to check if this modeling method can be used to generate the seed particles that are necessary for realistic modeling of gamma-ray glows. The first step for verifying our tool has been to check the propagation of protons between altitudes 50 km and 10 km above mean sea level (MSL). The further plan has been to check the propagation of electrons, positrons and gamma-rays between 20 km and 10 km and how these distributions change with a varying electrical field.

The check of propagation for protons has been completed between 50 km and 10 km. And the results show good agreement between the energy spectra and number of particle counts in the energy range $10^4 - 10^6$ MeV, while lower energies consistently is under estimated in the GEANT4 tool compared to the PARMA database. Since consistent results have not been reached for the reproduction of the proton distribution the work of comparing electron, positron and gamma-ray distributions have not been completed and is therefore left for future work.

Contents

List of Figures

List of Tables

List of abbreviations

ADELE Airborne Detector for Energetic Lightning Emissions

AU Astronomical Unit

BCSS Birkeland Centre for Space Science

CA Cloud-to-air

CC Cloud-to-cloud

CG Cloud-to-ground

EAS Extensive Air Shower

GCR Galactic Cosmic Rays

GEANT4 Geometry and tracking 4

GV Giga volt

IC Intra cloud

ILDAS In-Flight Lightning Damage Assessment System

keV Kilo electron-volt

kV Kilo volt

LSQ Least Squares

MATLAB Matrix laboratory

MC Monte-Carlo

MCS Mesoscale convective system

MeV Mega electron-volt

MOS Modification of Spectra

MSL Mean sea level

NCAR National Center for Atmospheric Research

PARMA PHITS-based Analytical Radiation Model in the Atmosphere

PHITS Particle and Heavy Ion Transport Code System

R_c Effective geomagnetic cutoff rigidity

R_L Lower geomagnetic cutoff rigidity

R_U Upper geomagnetic cutoff rigidity

RREA Relativistic Runaway Electron Avalanche

STP Standard temperature and pressure

TEB Terrestrial Electron Beam

TGE Thunderstorm Ground Enhancement

TGF Terrestrial Gamma-Ray Flash

TeV/n Tera electron-volt

W Wolf number

Chapter 1

Introduction

Lightning physics is a field where there still are many processes that are not well understood. According to *Dwyer et al.* (2012) many questions remain regarding electrification of thunderclouds, discharge mechanisms, lightning initiation, compact intracloud discharges, the global electrical circuit, transient luminous events and terrestrial gamma-ray flashes (TGF).

Changes to the scientific field of lightning physics followed with discoveries that thunderclouds, lightning and long laboratory sparks in air produce energetic runaway electrons with accompanying gamma-ray emissions. The emerging field of High-Energy Atmospheric Physics includes among other the measurement data from satellites of bright bursts of mega electron-volt (MeV) gamma-rays hundreds of kilometres away from the source. These data can be used together with information about lightning discharges to study how they are related. This field of study impacts traditional atmospheric electricity and lightning physics and it has also implications for the study of cosmic-ray extensive air showers, discharge physics, space physics, plasma physics and aviation safety.

Relevant manifestations of phenomena of gamma-ray production in thunderclouds that are currently being studied by research groups around the world are among others: TGFs, Terrestrial electron beams (TEB) and gamma-ray glows. The TGFs are millisecond duration flashes containing high energy photons of energy range MeV. TEBs are relativistic electrons launched into space, generated by TGFs. The term glow or gamma ray glow refers to any high-energy photon emission from a thundercloud that has a time scale longer than 1 second, longer than the time scales for TGF and lightning discharges. These emissions have a lower x-ray emission increase above background than the TGF phenomena. The described phenomena are poorly understood and they are the subject of intense studies around the world.

Measurements of high-energy radiation from thunderclouds were conducted with airplane flights in the 1980's [*Parks et al.* (1981) and *McCarthy and Parks* (1985)]. In the 1990's balloons were flown through and above active cells [*Eack et al.* (1996b), *Eack et al.* (1996a) and *Eack et al.* (2000)]. Further aircraft campaigns followed in the period 2009-2020 [*Kelley* (2014), *Kochkin et al.* (2017), *Østgaard et al.* (2019)].

Since *Wilson* (1925) developed the theory of relativistic runaway electrons in 1925 many advances in the theory of this process has been made. This research has largely been driven by the need to explain the production of the gamma-ray radiation as seen in TGFs. The details of the development stages with introduction of run-away avalanches [*Gurevich and Milikh* (1999)] and relativistic feedback [*Dwyer* (2003)] will be further explained in the background section of this thesis. Two production scenarios of Gamma-ray glows have been proposed. One involves Relativistic Runaway Electron Avalanche (RREA) process inside the thundercloud with seed cosmic ray electrons combined with electric fields that create conditions for relativistic electron runaway, multiplication and feedback. The other is a modification of spectra (MOS) where the required field strength is different than for the RREA process and the energy spectrum of the radiation is also different [*Chilingarian et al.* (2014)]. The MOS mechanism does not involve relativistic runaway for the electrons. These two production scenarios will be further explained in the background section of this thesis.

This thesis has the following chapters: 1: Introduction, with an introduction to the field of high energy atmospherics physics and lightning physics. 2: Background, with the theoretical background for lightning and electromagnetic processes involved in the production of hard radiation from thunderclouds. 3: Observations, a summary of previous observations of gamma ray glows from thunderclouds as well as modeling work for the investigation of possible production mechanisms. 4: Monte Carlo Models, with descriptions of the Monte Carlo (MC) models that have been used during the work for this thesis. 5: Methodology, how the MC models have been used, boundary conditions, interfaces and geometry. 6: Results, the results from the simulation work. 7: Discussion, the simulation results will be discussed here. 8: Future work. 9: Summary of the thesis with conclusions drawn from the work.

The goal of this thesis is to use sophisticated MC modeling tools to explore the production scenarios for gamma-ray glows.

Chapter 2

Background

This chapter gives a brief introduction to thunderstorms, lightning and the high energy physics processes related to the modeling work that will be described later in this thesis.

2.1 Thunderclouds

According to *Krehbiel* (1986): The difficulty in determining how thunderclouds become electrified lies in the fact that they are large, complex and short lived phenomena that need to be examined both as a whole and in detail in order to understand how they function [*Rakov and Uman* (2003)]. The electrical processes are intimately related to the cloud dynamics of motions and to the micro-physics of the cloud.

The primary source of lightning is cumulonimbus clouds. For this type of cloud to form there needs to exist moisture, an unstable air mass and a lifting force (heat). The cloud forms through the stages of cumulus, when small parcels of warm moist air rise and cool by adiabatic expansion. The cooling parcel that exceeds saturation lead to moisture condensing on air born particulate matter and forming the lower visibility boundary of the cloud. In order for the cumulus cloud to mature into a full grown cumulonimbus cloud the air has to be sufficiently warm and moist. The mature state of a thundercloud is denoted by cumulonimbus incus or anvil cloud. The thundercloud has reached stratospheric stability and has formed the characteristic flat anvil form of the cloud top.

On warm summer days clouds can be observed forming over warm land areas, the rising moist air condenses into cumulus clouds that grow into tall cumulonimbus clouds, which later can dissipate with thunderstorms and rain or hail. This development can be seen in Figure 2.1.

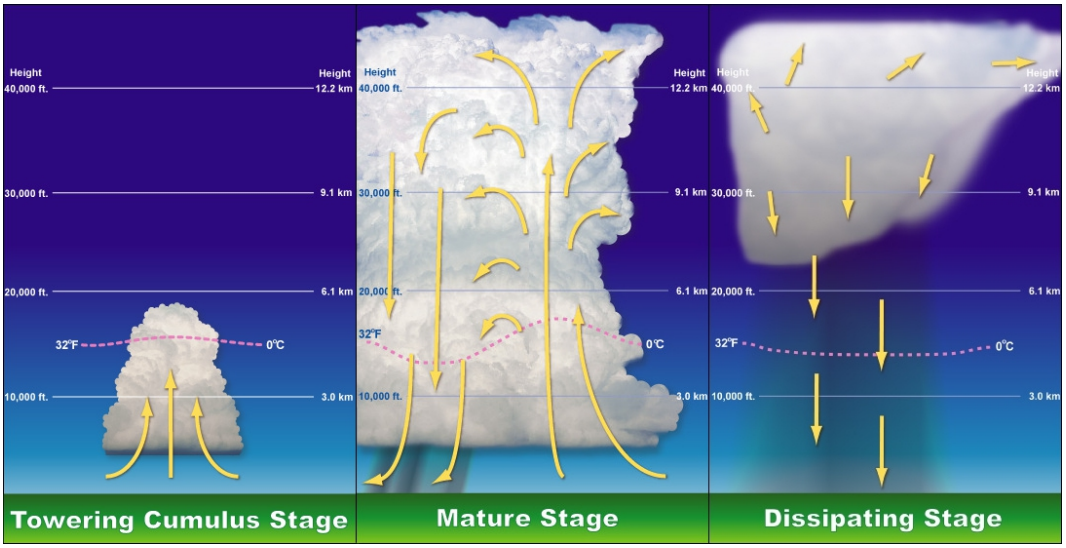

Figure 2.1: Stages of thundercloud growth. Towering cumulus develops to the mature stage of cumulonimbus which later dissipates. Figure from Wikimedia Foundation (2021).

2.1.1 Electrification of thunderclouds

A hydrometeor is any water or ice particle that have formed in the atmosphere or at the earths surface as a result of condensation or sublimation. According to *Rakov and Uman* (2003) the electrification of thunderclouds requires two processes. There must be a small scale process that can electrify individual hydrometeors and a process that spatially separates the charged hydrometeors in order to create a charge separation in the thundercloud. Most of the charge rests on hydrometeors of relatively low mobility, which leads to the cloud being a relatively good insulator.

The mechanisms for thundercloud electrification are not fully understood, but the growing consensus is that the graupel-ice mechanism is the dominant method for electrifying thunderclouds. Here we will give a brief introduction to this mechanism.

Graupel-ice mechanism

The production of electric charges by this mechanism is provided by collisions between precipitating particles (grauple) and cloud particles (small ice crystals). Precipitating particles are here defined as hydrometeors that have a fall speed higher or equal to 0.3 m/s. By this mechanism the charge separation is provided by gravity.

The electrification of the individual particles involves collisions between grauple particles and ice crystals in the presence of water droplets. Significant charge transfer requires the presence of water droplets. Figure 2.2 illustrates the mechanism. In the figure the bigger grauples falls through the surrounding ice crystals and water droplets. The droplets will remain in a supercooled liquid state until they contact an ice surface, then they freeze and attach to the surface.

When the temperature is below a critical value T_r the falling grauples will acquire

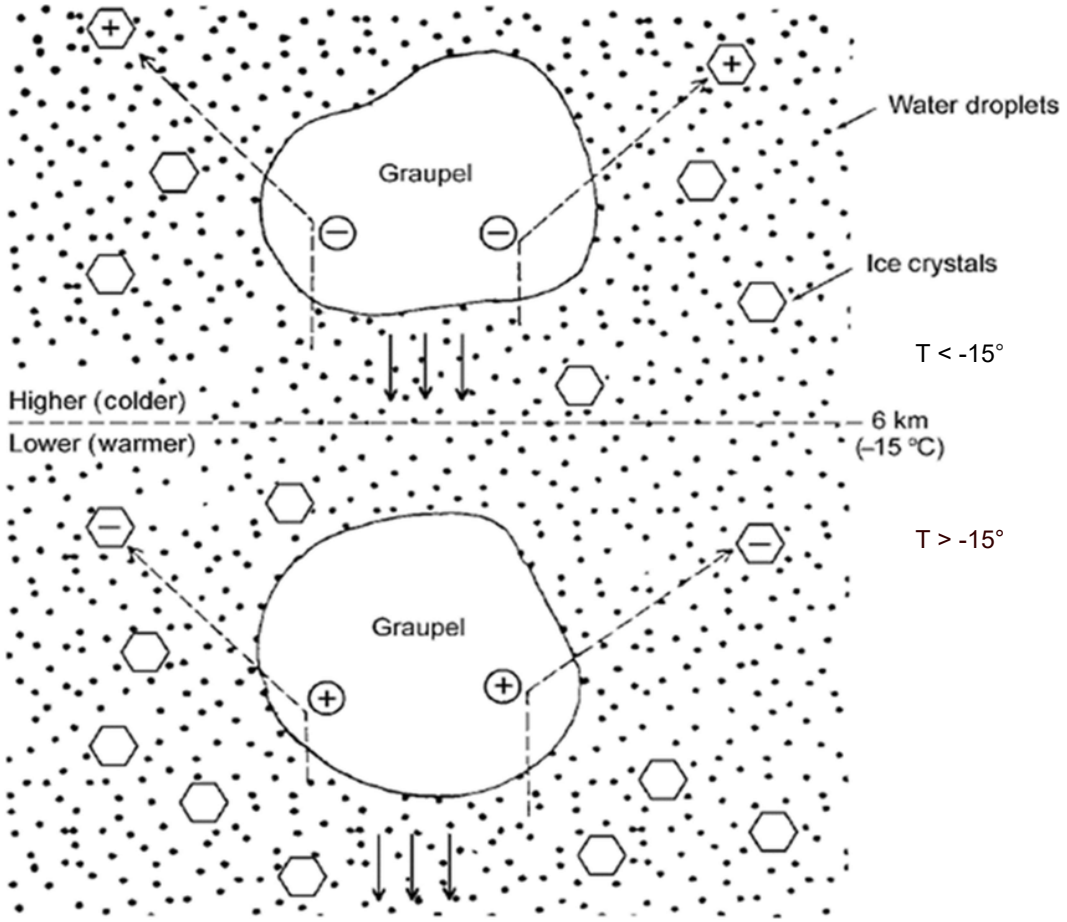

Figure 2.2: Electrification of thunderclouds with the graupel-ice mechanism. It is assumed that the reversal temperature T_r is -15°C and that it occurs at a height of 6 km. Figure adapted from Rakov and Uman (2003).

negative charge in collisions with the ice crystals. At temperatures above T_r they acquire a positive charge. The charge sign reversal temperature T_r is generally thought to be between -10°C and -20°C. Graupels that fall below the altitude of T_r picks up positive charge and form the lower positive charge layer of the thundercloud.

2.1.2 Charge structure

Thunderstorm charges reside mainly on hydrometeors, but some are also ions. The structure of the charges is complex and it changes during the maturation of the thundercloud. The simplified model of a thundercloud charge structure can be seen in Figure 2.3. This model is called the tripole structure and in the figure the three main charge layers are represented as point charges with vertical separation. The main charge layers of a thundercloud is the upper main positive charge layer, the middle main negative charge layer and the lower positive charge layer. The two main charge layers are often modeled with equal charge magnitude.

According to *Stolzenburg et al.* (1998) the charge structure of thunderclouds as inferred from 50 balloon electric field soundings have different charge structures for dif-

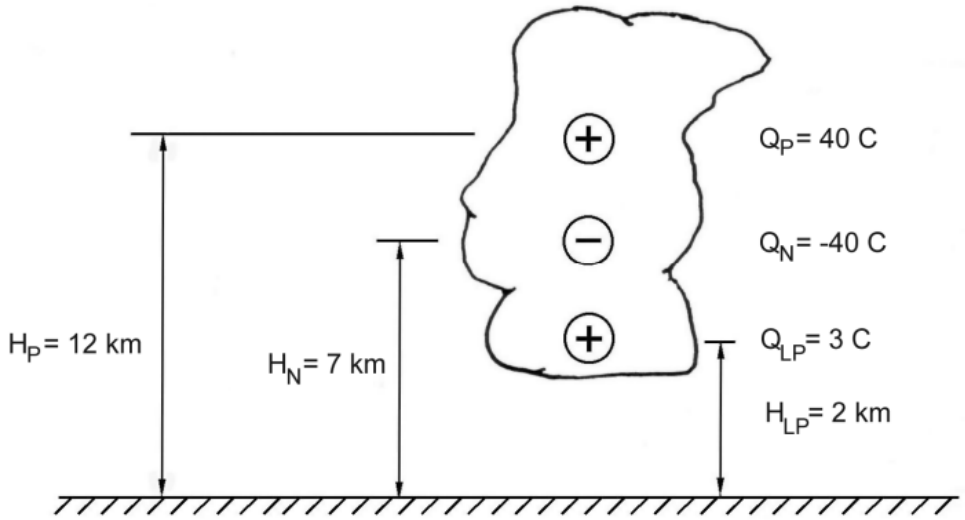

Figure 2.3: A modeled simplified charge structure in a thundercloud. In this figure three point charges represents the charges structure of a thundercloud. The main upper charge layer is modeled as a point charge with 40 C charge, the negative screening charge layer is modeled as a -40 C point charge and the lower positive charge layer is represented by a 3C point charge. Such a model can be used to calculate an estimated electrical field associated with a thundercloud, the charges in the cloud will be distributed over an area not localized to point charges. Figure from Rakov and Uman (2003).

ferent types of clouds. They analyzed soundings from updrafts of mesoscale convective system (MCS), isolated supercells and isolated New Mexico mountain thunderclouds. In updrafts of MCS convective regions, in strong updrafts of supercells and in or near the center of convection in New Mexican thunderclouds four charge regions were identified. The four regions can be seen as the classical tripole structure of a thundercloud plus an upper negative screening layer. Outside the updrafts of MCS convection regions, outside strong updrafts of supercells and away from the center of convection in New Mexican thunderclouds a more complex charge structure with six charge layers were identified. The lower layer was positive, these structures can be seen in Figure 2.4.

The 4 pole charge structure described by *Stolzenburg et al.* (1998) has a negative screening charge layer in addition to the simplified tripole structure. Screening charge layers form on all surfaces of a cloud boundary with opposite charge from the charge layers inside of the thundercloud. According to *Rakov and Uman* (2003) the negative upper and positive lower screening charge layers are well documented by observations, but the screening charge layers of the side of the clouds are harder to observe.

2.1.3 Electric field

The electric field is a property associated with points in space when charge is present in any form. The magnitude and the direction of the electric field are expressed by the value E. In the case of a point charge a positive field points radially outward from the positive charge or radially inward towards the negative charge. With more charges

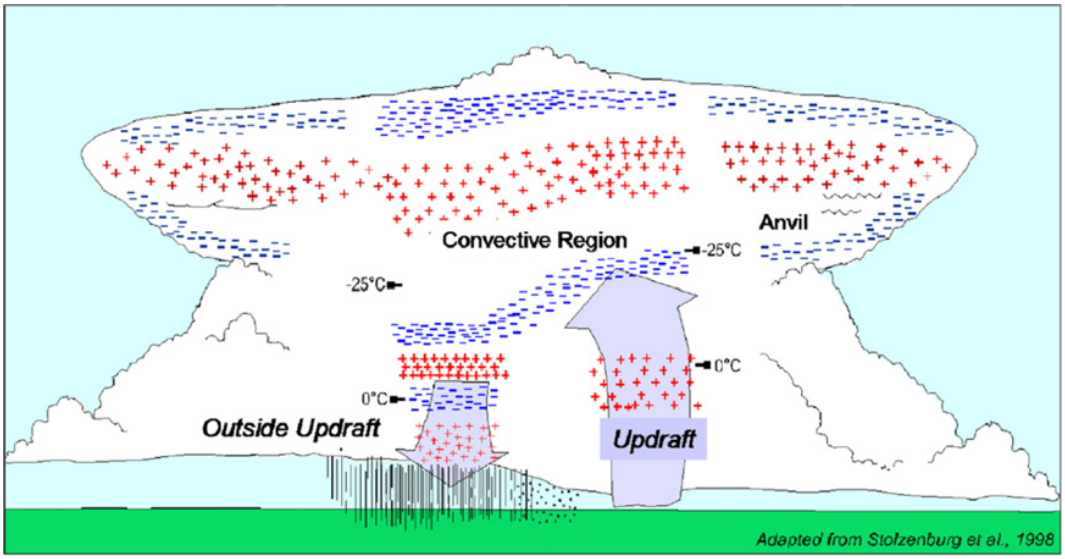

Figure 2.4: Schematic of charge structure in convective region of a thunderstorm. Four charge layers are seen in the updraft region, and six charge layers can be seen outside the updraft region. This charge structure applies to the convective elements of MCS. Figure from Rakov and Uman (2003).

present the electrical field at a specific point will be the summed effect of all relevant charges at that point. In order to determine the effects of the electrical field on a test charge it is only required that we have knowledge about the value of the field and not what produced it. For thunderclouds this means that the value of the electrical field is sufficient to determine the electrical force experienced by a charged particle at that point.

The force F_e on a charged particle q_0 in an electric field E is given by Equation 2.1.

$$F_e = Eq_0 \; [N] \tag{2.1}$$

The electrical field inside of a thundercloud can be regarded as a quasi-static field, meaning that it varies much slower than the process we study. In our simulations we will be using a uniform electric field between the main negative and the main positive charge region inside the thundercloud.

The electrical field of a thundercloud is dependent on the type of cloud and the maturation. The thundercloud contain different charge regions that contributes to a varying electrical field with altitude and horizontal position within the cloud. This means that the actual electrical field of a thundercloud is difficult to predict and that field measurements are needed in order to determine the actual field strength at a given position.

2.1.4 Lightning

There are several different forms of lightning discharges and they are classified according to their start and end location as follows: cloud-to-ground (CG), intra cloud (IC), cloud-to-cloud (CC) and finally cloud to air (CA). The most common type of discharge

is the IC and according to *Rakov and Uman* (2003) they constitute 75% of all lightning discharges. The second most common is the CG discharge while the two last types are relatively uncommon.

Gamma-ray glows are thought to originate independently of lightning discharges and therefore initiation and propagation of lightning is not the topic of this thesis. For a good review of this topic it is recommended to read Chapter 4 from *Rakov and Uman* (2003).

2.2 Particle interactions

This section is intended to give the reader a brief introduction into the different particle interactions that are relevant in the field of high energy atmospheric physics related to gamma-ray glow emissions from thunderclouds.

The particles most relevant for our simulations are electrons, positrons and photons. These particles undergo several interactions when in the vicinity of atmospheric nucleus/atoms that are relevant for the propagation, multiplication and creation of these particles. Prior to descriptions of these processes the reader will be given a brief introduction to cosmic ray particles which in the modeling work later in this thesis is thought to be the source of atmospheric electromagnetic particles.

2.2.1 Cosmic ray particles

Astronomer Carl Sagan once said: "The nitrogen in our DNA, the calcium in our teeth, the iron in our blood, the carbon in our apple pies were made in the interiors of collapsing stars. We are made of starstuff". Understanding cosmic rays and their origin can help us to answer fundamental questions about the beginning of the universe, its evolution and about our own existence.

Cosmic ray particles are the most energetic particles ever observed. Their energies can exceed 10^{14} MeV. Little is known about their origins and they have been studied since the early 20th century. The particles come in a wide range of energies, the energy distribution is approximately given by Equation 2.2:

$$\frac{dN}{dE} \propto \frac{1}{E^3} \tag{2.2}$$

Where N is the number of cosmic ray particles and E is their energy respectively. This relation between energies holds with reason between 10^7-10^{17} MeV, with a slight change of slope at 10^9 and 10^{13} MeV. The current scientific consensus is that cosmic rays bombard the earth completely uniformly in space, time and direction. The lower energy cosmic rays are deflected by the earths magnetic field.

The geomagnetic cutoff rigidities are a quantitative measure of the shielding provided by the earths magnetic field. According to *Smart and Shea* (2005) the accepted

manner for determining cut off rigidities is to trace particles in a current International Geomagnetic Reference Field model combined with a model magnetosphere. There is no single number that completely describes the geomagnetic cutoff rigidity. For each position and in each direction there are three distinct quantities to describe the geomagnetic cutoff: (R_U) Upper geomagnetic cutoff rigidity, (R_L) Lower geomagnetic cutoff rigidity and (R_C) Effective geomagnetic cutoff rigidity. The effective cutoff value is used for many applications where a simple value for cutoff rigidity is desired. Particles with lower rigidity than R_C cannot reach the given location. The most protected region is the equatorial region and according to *Mironova et al.* (2015) particles must posses rigidity of 13-17 giga volt (GV) to be able to reach the atmosphere here, while the polar regions have no shielding.

The solar activity influences the flux of galactic cosmic rays in an inverse manner [*Buchvarova et al.* (2003)]. Galactic cosmic rays have important influence on the solar-terrestrial relations during solar minimum and solar cosmic rays during solar maximum. The solar activity can be measured by the number of sunspots, which are temporary phenomena on the sun's photosphere. Sunspots appear as spots darker and have lower temperature than the surrounding areas because of inhibited convection due to concentrations of magnetic flux. The sunspot number varies according to the approximately 11 year solar cycle. The solar activity index or Wolf number (W) measures the number of sunspots and groups of sunspots present at the surface of the sun.

The cosmic ray particles incident on the earth atmosphere consists mainly of protons, alpha particles and heavy ions. The dominant fraction of the primary cosmic rays are protons, with the second largest fraction alpha particles constituting about 10% by particle number, other nuclei make up less than 1% [*Mironova et al.* (2015)]. As the particles propagate through the atmosphere they interact with the other molecules present there. The heavier fractions of the cosmic ray flux will have shorter interaction lengths than the lighter protons and therefore lose energy faster [*Stanev* (2010)].

Three types of interactions occur for cosmic rays: 1.) electromagnetic interactions of charged particles (relevant for our simulations of secondary electrons, positrons and photons). 2.) inelastic hadronic interactions that are important for the production of secondary particle fluxes. 3.) nuclear interactions, heavier nuclei are split into lighter ones. Which is most important for changes of chemical and isotropic composition of accelerated cosmic ray nuclei. In lower altitudes, which is where we are intending to investigate the phenomena of gamma ray glows from thunder clouds, the cosmic ray particles are mostly secondary particles, produced by interactions between primary particles and the atmospheric molecules.

The flux of cosmic ray particles are in this thesis referred to either as omnidirectional or angular. Omnidirectional-flux includes the flux from all zenith angles, while directional flux is specified as the flux that crosses a horizontal surface at the specified angle. The units for differential omnidirectional flux as stated in Equation 2.3 is given as number of particles per square centimeter per second and they are given per nucleon for ions. For the differential directional fluxes in Equation 2.4 the units are also given

per steradian (solid angle).

$$\frac{1}{cm^2\, s\, (MeV/n)} \tag{2.3}$$

$$\frac{1}{cm^2\, s\, (MeV/n)\, sr} \tag{2.4}$$

2.2.2 Cross section

Cross sections are the measure of the probability that a specific process will take place, under specific conditions. It is a relation between two particles or a particle and a target.

An example is an electron travelling through a gas consisting of atoms and molecules. The electron can transfer energy to the other particles in the gas, the amount of energy being dependent on the nature of the collision. Elastic collisions conserves the kinetic energy of the electron, but changes its direction. Inelastic collisions will transfer some of the kinetic energy to surrounding particles which can excite or ionize atoms.The probability of a collision is dependent on the given particle and the nucleus/atom involved in the collisions as well as their specific energies.

The cross section σ is the probability for a particle to interact with the medium. The expression for cross section is given by Equation 2.5, where r is the number of interactions with the nuclei with density n_t, n_p is the density of the incident particles and A is the area.

$$\sigma = \frac{r\, n_t\, A}{n_p}\, [m^2] \tag{2.5}$$

Determination of cross sections is a complicated process that involves several aspects. The cross section for a single reaction is called the partial cross section and the sum of all the relevant cross sections is called the total cross section. Relating to the total cross section is the mean free path which is the average distance traveled between each collision or interaction. The expression for mean free path is given in Equation 2.6 and has the unit of [m]. Here the molecular number density is given by n and σ is the total cross section with dimension area.

$$\lambda = \frac{1}{n\, \sigma}\, [m] \tag{2.6}$$

2.2.3 Photon production processes

The predictions of classical electromagnetic theory is that an accelerated charged particle emits electromagnetic radiation. Acceleration of a charged particle in the columb-field of an ion is an example of this. The change in momentum is accounted for by the emission of a gamma-ray particle.

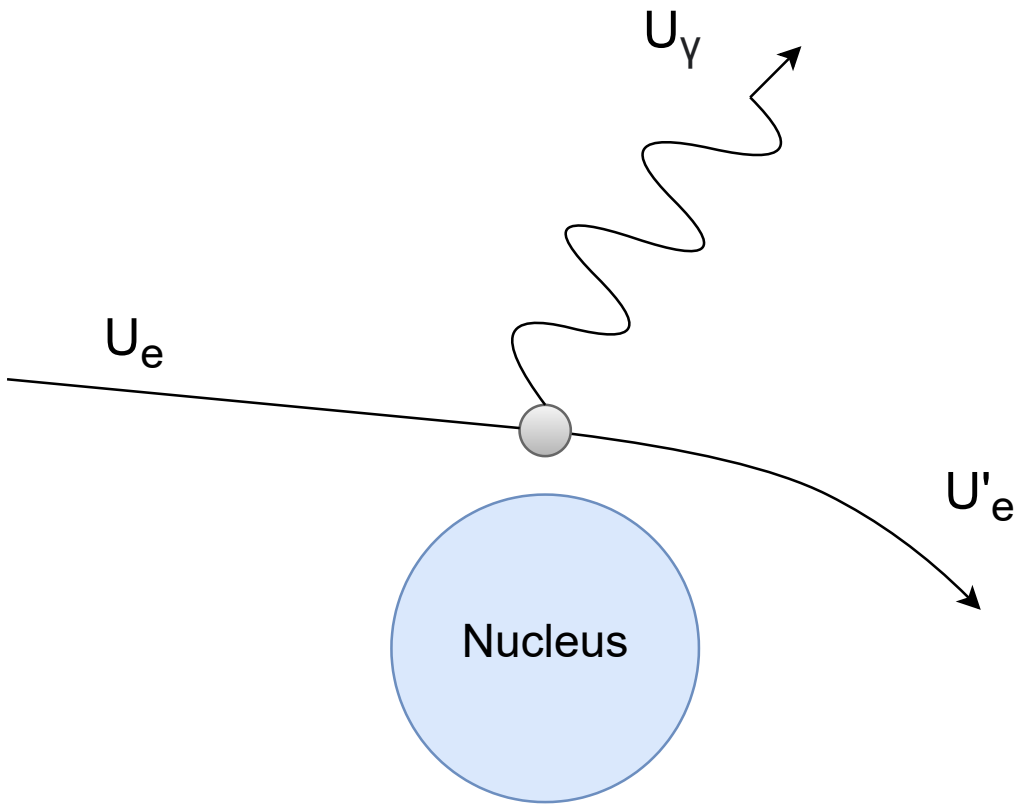

Figure 2.5: Bremsstrahlung, an incidence electron with energy U_e deflects and loose energy in the Coulomb field of a nucleus. The energy is released in the form of a photon with energy $U_\gamma = hf = U_e - U'_e$.

Bremsstrahlung

Bremsstrahlung is one of the most important energy loss processes for electrons. The process also occurs for positrons, but this is less common due to the relative larger abundance of electrons compared to positrons.

The process of bremsstrahlung "breaking radiation" in which a charged particle is decelerated by another charged particle, by example an electron in the Coulomb field of a nucleus as shown in Figure 2.5. The electron in our example will emit electromagnetic radiation in the form of photons as it is retarded and deflected by the Coulomb field of the nucleus. The radiation energy is of magnitude such that energy is conserved in the process. The process has a continuous energy spectrum with higher frequency photons corresponding to higher deceleration of the electron.

2.2.4 Photon interaction with matter

This section will describe the processes that are relevant for the interaction of photons with matter in the terrestrial atmosphere. Since photons do not have charge they do not undergo inelastic collisions with electrons. The interactions that will be described here are: photoelectric absorption, Compton scattering and pair production. The cross

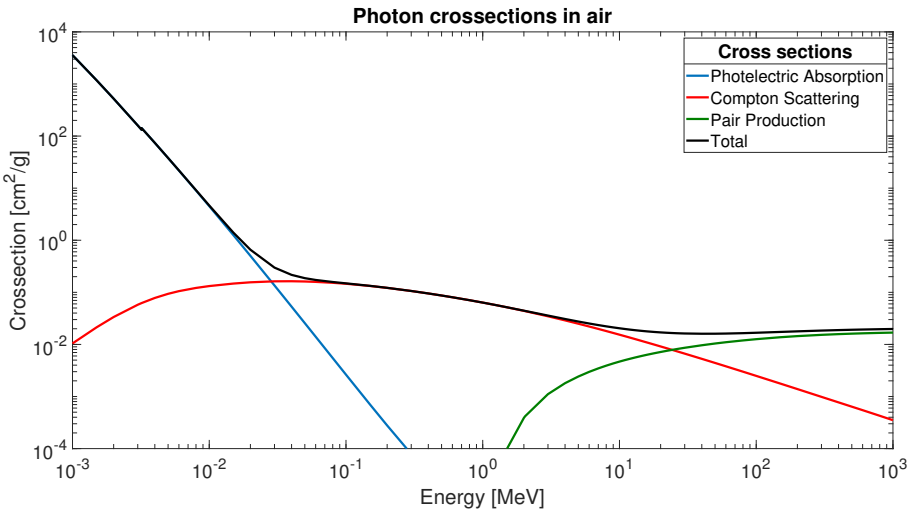

Figure 2.6: Cross-sections for photon in air dependent on energy. Black curve represents the total cross-section, photoelectric absorption (blue), compton scattering (red) and pair production (green). Units for cross-section is given in $[cm^2/g]$. Figure made with data from National Institute of Standards and Technology (NIST) XCOM database [M.J.Berger et al. (1998)].

sections for these interactions depend on the energy of the incident photon and as we can see in Figure 2.6 the lower energy photons have a higher probability for undergoing photoelectric absorption, middle energy photons have higher probability to undergo Compton scattering and high energy photons are most likely to undergo pair production.

Photoelectric absorption

In this process the photon is absorbed by an atom, which ejects an atomic electron in the process. The required energy to remove an electron from an atom is denoted U_b (binding energy of the electron), the remaining energy from the incident photon is converted to kinetic energy of the ejected electron. The energy of the incidence photon is given by hf where h is planks constant and f is the frequency of the photon. The recoil momentum for the reaction is absorbed by the nucleus to which the electron was bound.

$$(\frac{1}{2}mv^2)_{max} = hf - U_b \tag{2.7}$$

The maximum kinetic energy of the ejected electron can be found by subtracting the binding energy of the electron from the energy of the photon as shown in Equation 2.7. The interaction is sketched in Figure 2.7.

Compton scattering

Compton scattering involves free electrons or electrons in which the incident photon has a much higher energy than the binding energy of the electron. During Compton scattering the electron is scattered away along with a new photon of lower energy than the incident photon. In this thesis we will not discuss Rayleigh scattering which is the

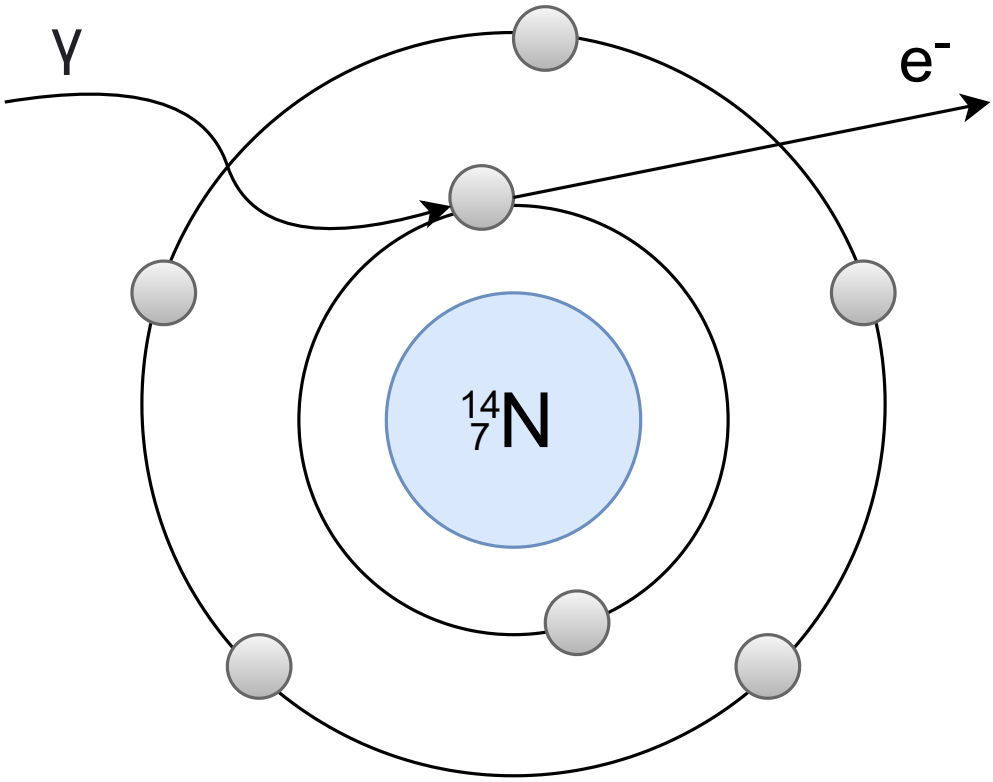

Figure 2.7: Photoelectric absorption, an incident photon ejecting an electron from an atom.

process where a photon interacts with a whole atom in which the incoming photon is deflected and only applies to low energy photons.

The expression that relates the wavelengths of the incident and scattered photons and the scattering angle of the photon is called Compton's equation. This expression is found by applying the laws of conservation of momentum and energy in relativistic form for calculation of the change in wavelength or energy of the incident and the scattered photon.

$$\lambda_f - \lambda_i = \frac{h}{mc}(1 - cos\omega) \tag{2.8}$$

In Equation 2.8 the change in wavelength is only dependent on the scattering angle ω as the constant $\frac{h}{mc}$, known as the Compton wavelength of the electron is constant.

Compton scattering is the dominant process for photons in air of energies between 30 kilo electron-volt (keV) and 20 MeV. At energies lower than 30 keV photoelectric absorption dominates. Above 20 MeV the dominant process is pair production.

Pair production

Pair production is the process in which an electron/positron pair materializes from a pulse of electromagnetic energy (a photon). It is a direct conversion of radiant energy to matter and the process usually takes place in the vicinity of a nucleus. The process is one of the principal ways in which high-energy gamma rays are absorbed in matter. In order to produce the particle anti-particle pair the photon must have an energy of

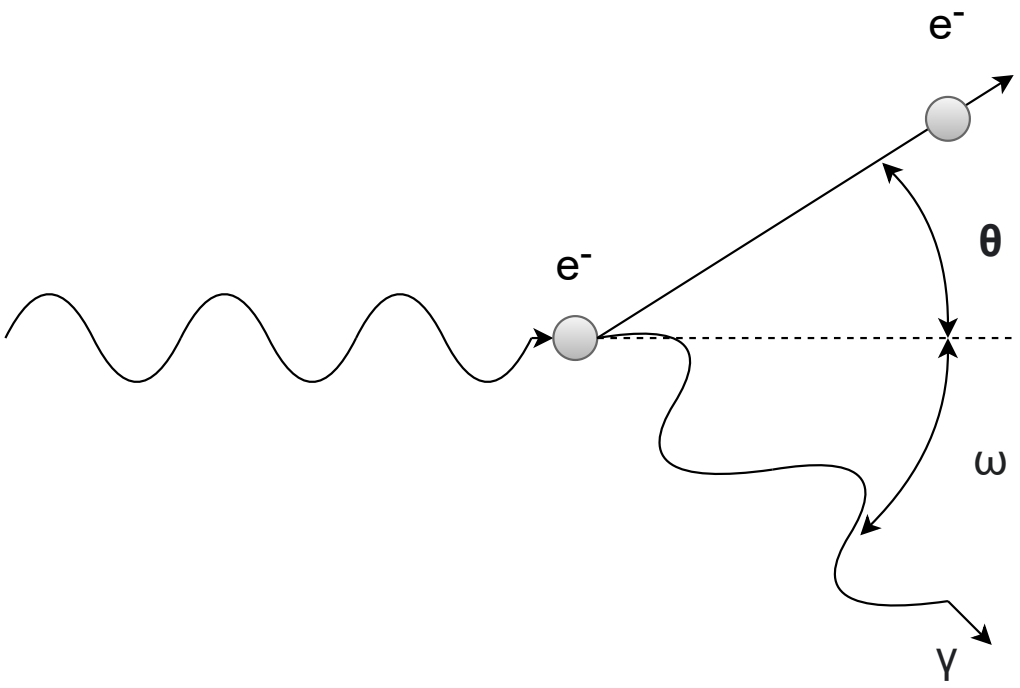

Figure 2.8: Compton scattering, an incident photon ejecting an electron and a scattered photon.

minimum 1.022 MeV equal to the rest mass of the particles. The energy requirement follows from Albert Einsteins famous equation $E = mc^2$.

The remaining energy after formation of the particles is converted to kinetic energy for the electron and positron. Therefore a higher energy photon will produce higher energy electron positron pairs. In Figure 2.9 the process is visualized schematically.

$$E_k = hf - 2m_e c^2 \tag{2.9}$$

The kinetic energy E_k shared between electron and positron is given by the expression in Equation 2.9 as the difference between the photon energy hf and the rest mass of the electron positron pair $2m_e c^2$.

2.3 Glow production processes

As mentioned in the introduction to this thesis there has been proposed two different theories to describe the production of gamma-ray glows from thunderstorms. The two are differing in that one, RREA requires a higher field strength and therefore is assumed to occur within the high electric field area inside of the thundercloud. The other, MOS requires a lower field strength and can therefore also be initiated in layers of the thundercloud with lower electrical field magnitude.

There is a distinct difference in spectrum between the two production processes, that is visualized in Figure 2.10. Here the changing spectrum with higher electric field can be seen. The higher increase of flux at the lower end of the energy spectra signify that the RREA process is producing runaway electrons. In this section an introduction

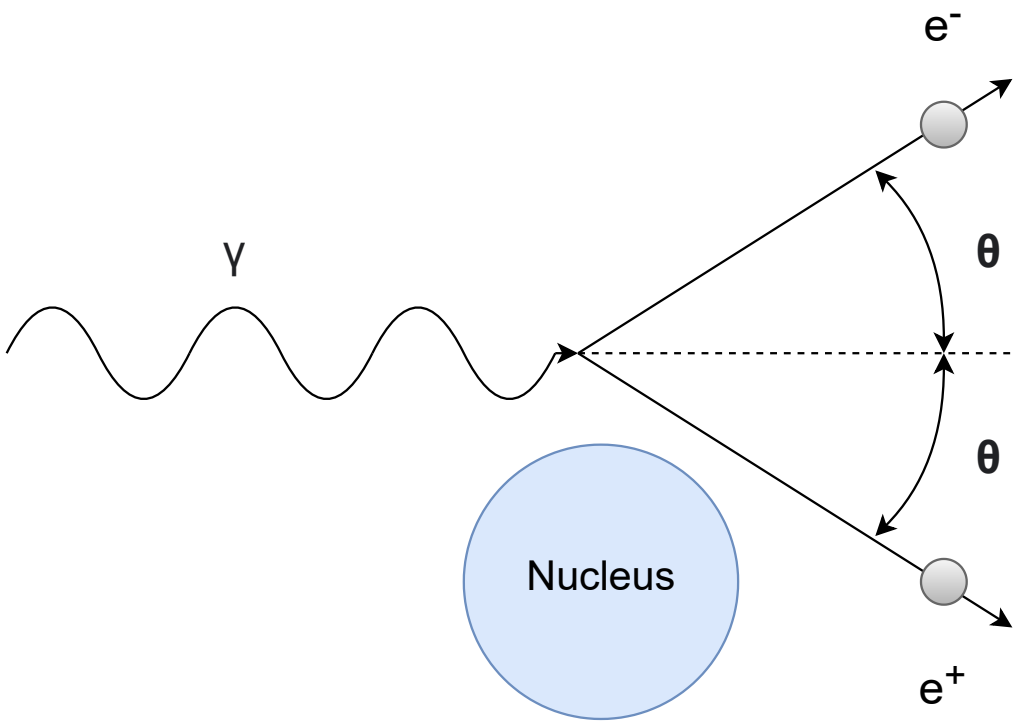

Figure 2.9: Pair production, an incident photon with energy hf interacts with a nucleus and produces a electron positron pair. The total energy and momentum is conserved in the process, therefore the kinetic energy of electron and positron combined equals the energy of incident photon subtracted the particle pairs rest mass.

to the two production mechanisms with their respective theoretical developments will be given.

2.3.1 Relativistic runaway electron avalanche

In 1925, C.T.R Wilson developed the theory of the runaway electron [*Wilson* (1925)]. The idea behind the theory is that energetic electrons in air can gain high amounts of energy from static electric fields resulting in an increase in x-ray radiation from bremsstrahlung as the electron energy increases.

In Figure 2.11 we can see the value of the frictional force that electrons experience at standard temperature and pressure (STP) given for increasing electron energy. The curve has a peak at E_c, which corresponds to the thermal runway field, which is the field threshold for thermal electrons to accelerate to higher energies. The frictional force for higher energy electrons drop down until the relativistic field value E_t. A low energy electron will need a field of value of E_c if it is to accelerate past the peak of the friction graph and run away, while for higher energy electrons lower field values is sufficient. As can be seen in the figure the minimum field value in which an electron can run away is 2 kV/cm, note that the field value will be lower with decreasing air density. According to *Dwyer* (2003) the actual field value required for runaway is 30% higher due to elastic scattering and *Dwyer et al.* (2012) states that electric fields of magnitude close to E_t have been measured inside thunderclouds.

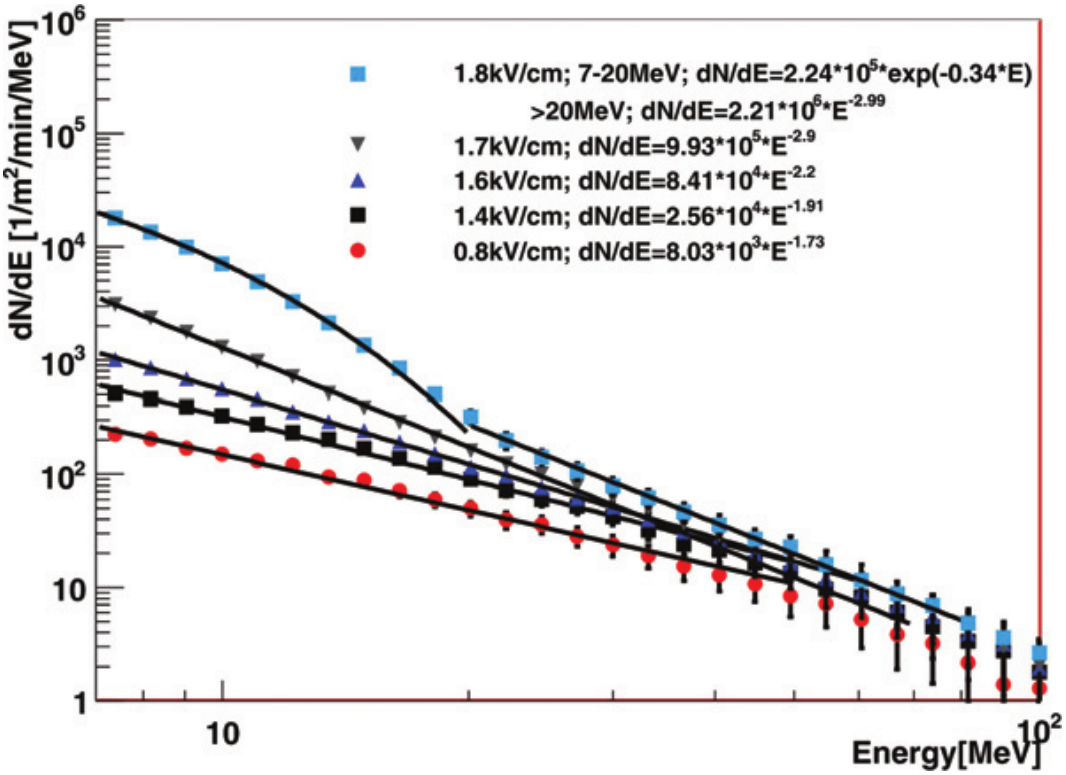

Figure 2.10: Differential energy spectra of gamma rays from a uniform electric field. The energy range of the radiation is 7-100 MeV and the electric field is varied to visualize the difference in energy spectra between MOS and RREA processes. The RREA process is initiated as the field increases. Figure from Chilingarian et al. (2014).

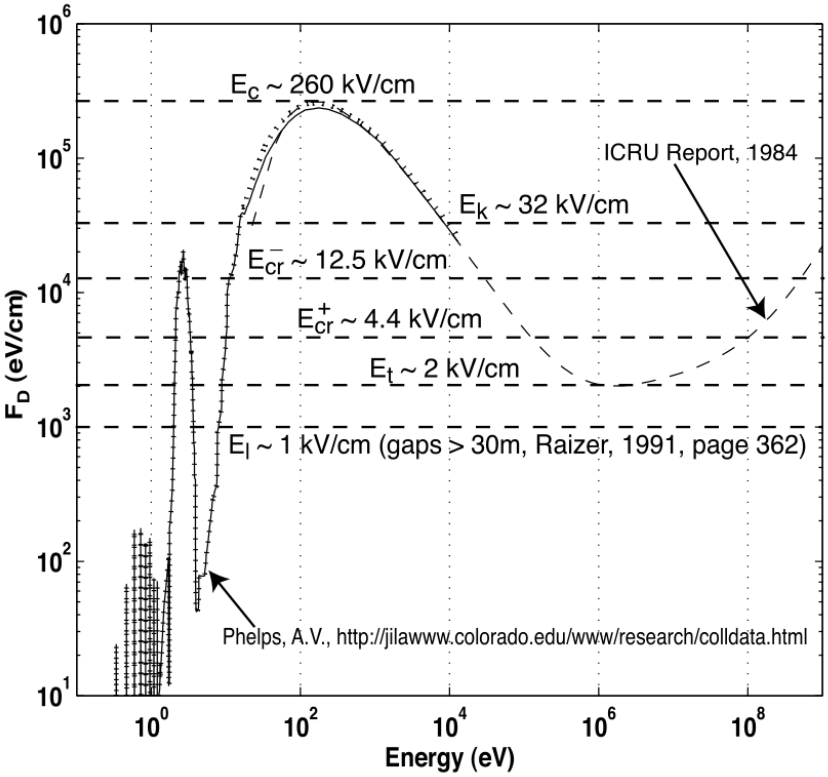

Thermal Runaway:	E_c ~ 260 kV/cm	Positive Streamer:	E_{cr}^+ ~ 4.4 kV/cm
Conventional:	E_k ~ 32 kV/cm	Relativistic Runaway:	E_t ~ 2 kV/cm
Negative Streamer:	E_{cr}^- ~ 12.5 kV/cm	Leader:	E_l ~ 1 kV/cm

Figure 2.11: Curve of dynamic friction force experienced by a free electron (or positron) moving through air as a function of kinetic energy at STP. Figure from Moss et al. (2006).

Wilson's theory explains how an energetic electron can run away in an electric field larger than E_t. When the electron gains sufficient energy it can interact and undergo bremsstrahlung thereby producing photons. This line of reasoning depends on the existence of a sufficiently strong electric field and electrons with sufficiently high energy. Energetic electrons in the atmosphere is known to originate from two separate sources: (1) cosmic rays secondary electrons or (2) radioactive decays. Due to the limited flux of these electrons Wilson's theory is not sufficient to explain phenomena like TGFs where the gamma-ray flux is larger than the theory is able to predict. Another possible source of energetic electrons is the electric fields in the streamer zone ahead of lightning leader tips. According to *Moss et al.* (2006) they can accelerate electrons to 2-8 kilo electron-volt (keV) and high potentials in streamer zones of lightning leaders can further accelerate the electrons to energies of hundreds of keV. This mechanism is not described in this thesis as observation have shown that lightning is more likely to terminate than initiate gamma-ray glows.

In 1992 *Gurevich et al.* (1992) showed that when one includes Møller scattering (electron-electron elastic scattering) in runaway electron simulations the energetic electron population will undergo a avalanche multiplication. The energetic electrons scatter with non energetic electrons which enables more electrons to runway, this phenomenon is termed RREA. The threshold field value for RREA was investigated by *Dwyer* (2003) which found it to be $E_{th} = 2.84x10^5$ V/m x n, where n is the density of air with respect to density at sea level. This value does not take into account the fact that the scattering of the electrons and the change they have in direction due to Coulomb interactions will lead to them not being fully aligned with the electric field lines. According to *Dwyer et al.* (2012) this leads to the requirement that the field value should be 30% larger in order to compensate for this effect.

Figure 2.12 shows an additional development step on the way to explaining energetic gamma-ray emissions from thunderclouds. *Dwyer* (2003) found that the back-scattering of photons during RREA can lead to the production of additional energetic electrons by Compton scattering or photoelectric absorption. These electrons contribute to the production of x-ray photons as they can propagate the high field region after production. Generally the high field region will have a limited length. This makes the back-scattering a useful mechanism in order to explain the x-ray production within this region. High energy photons from energetic electrons undergoing bremsstrahlung can produce electron positron pairs by pair production. The positrons that avoid electron-positron annihilation can accelerate rapidly in the opposite direction of the runaway electrons. As the cross-section of electron positron annihilation decreases rapidly with increasing positron energy, the positrons that run away can traverse to the start of the avalanche region and produce additional electrons via hard elastic scattering with atomic electrons in air (Bhahba scattering). These electrons can then produce secondary avalanches. These mechanisms are jointly referred to as relativistic feedback.

The development of the theories of RREA and relativistic feedback have largely been due to the effort to understand the TGF phenomenon. The mechanisms also help us to understand how the gamma-ray radiation as observed during gamma-ray glows can be produced. The requirements for production of the radiation is a sufficiently

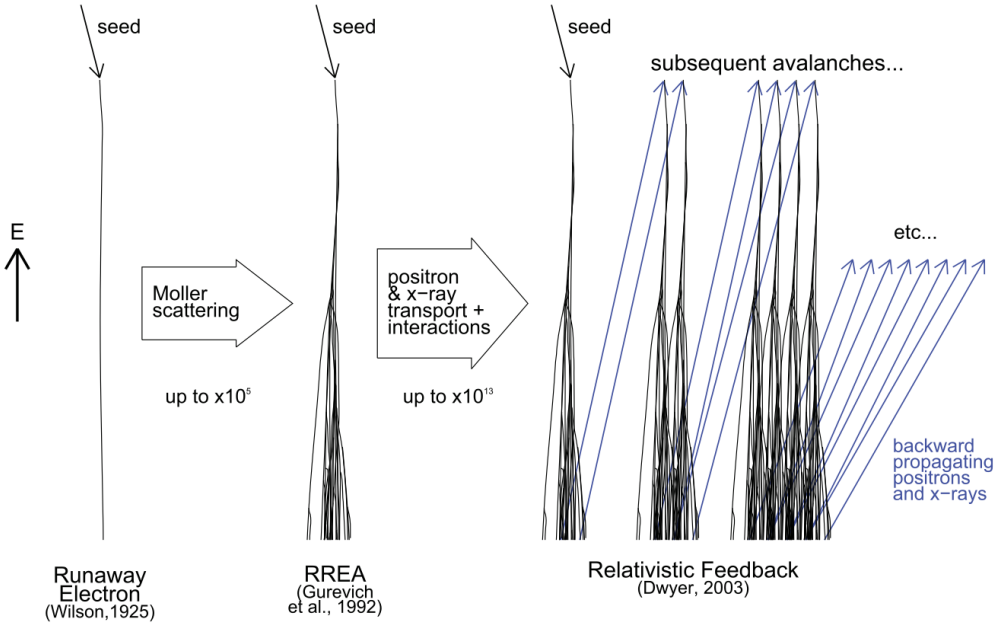

Figure 2.12: Schematic diagram summarizing the theoretical development for runaway electrons. Gurevich et al. (1992) supplemented Wilson's theory with the effects of Møller scattering. The scattering effects means that one energetic electron can avalanche to create 10^5 *energetic electrons. Dwyer (2003) discovered the feedback mechanism where back-scattering particles contributes to an additional multiplication factor of* $x10^{13}$*. Figure from Dwyer et al. (2012).*

strong electric field with sufficient vertical extent and a sufficiently large population of seed energetic electrons that undergo the described processes and multiply in order to produce a sufficient amount of energetic gamma-ray photons via the bremsstrahlung process.

2.3.2 Modification of specter

The MOS mechanism is opposed to the RREA mechanism in that it does not explain the increase in gamma-ray radiation by relativistic runaway of the electrons, but by a modification of the energy specter for cosmic ray electrons and positrons. The electric field strength required to initiate the MOS mechanism are a fraction of E_t (the strength required to initiate RREA). According to *Chilingarian et al.* (2014) electric fields provide additional energy to cosmic ray electrons resulting in a electron lifetime increase and additional path lengts in the atmosphere that increase the probability of x-ray production.

The increased gamma-ray flux can be detected as an increase above the background radiation. This increase is termed thunderstorm ground enhancement (TGE) by *Chilingarian et al.* (2014). According to *Chilingarian et al.* (2014) the energy spectra of the enhancements made by the MOS process is in the range 1-100 MeV. The MOS process is dominating for the energy range higher than 40 MeV, while RREA process generates gamma rays with energies below 40 MeV, though with a much higher intensity.

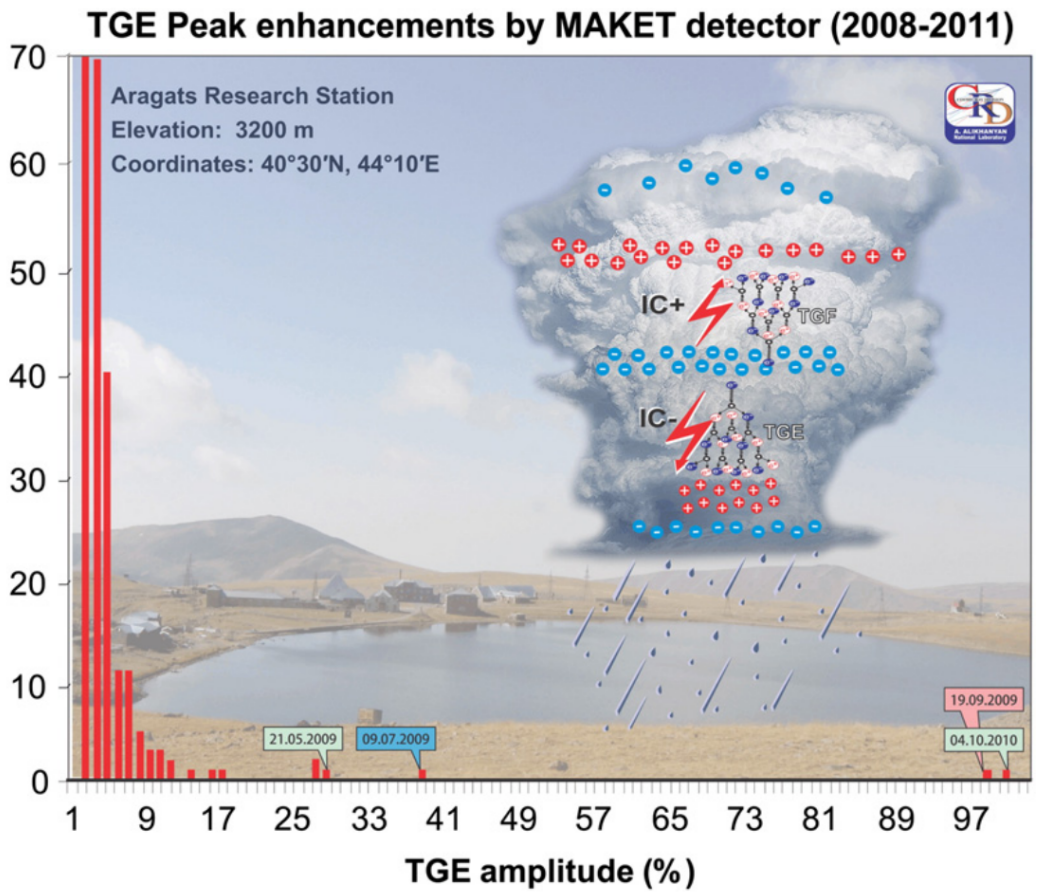

Figure 2.13: Histogram of amplitudes of TGE events as reported in Chilingarian et al. (2012). The figure illustrates possible production regions of TGF and TGE radiation. Figure from Chilingarian et al. (2012).

As can be seen in Figure 2.13 the relative abundance of lower TGE amplitudes, thought to be attributed to the MOS process is much larger than the high energy events as recorded in the ground based observatory in Aragats research station. The figure also shows where the proposed mechanisms are thought to originate. The RREA mechanism between main positive and negative charge region and MOS mechanism in the lower field between main negative and lower positive charge region. Note: The MOS mechanism is thought to be able to produce gamma-ray emission increases in all regions with sufficient electric fields and that the indicated position in this figure is due to the specific location for the meassuremets as described in *Chilingarian et al.* (2012).

2.4 Attenuation of particles in the atmosphere

The attenuation of massive particles and electromagnetic radiation in the atmosphere is due to different processes.

Photons interact in different processes as described in subsection 2.2.4, as can be seen from Figure 2.6 the higher energy photons are likely to pair produce. The middle energy photons will Compton scatter which reduces the energy of the photon and scat-

ters it while the lower energy photons are likely to be absorbed by an atom in photo electric absorption. The effects are all smaller higher up in the atmosphere where the lower abundance of molecules to interact with means that the photons will have a longer path-length. This explains why we can measure gamma-rays produced in thunderclouds with satellites orbiting the earth or by airplanes flying over the clouds. Measurements on the ground is also possible, but they are more likely to be influenced by local disturbance and also have higher attenuation by scattering and absorption in the higher density air below the thunderclouds. In higher altitudes ground based measurements will be easier to accomplish as the attenuation will be lower.

Electrons with high energy undergo bremsstrahlung as long as there is nucleus's to interact with. Lower energy electrons will experience friction and unless there is a field to provide accelerating force, they will slow down due to collisions. Some high energy electrons can escape upwards from thunderclouds and they will become trapped particles gyrating around the magnetic field lines. This can not happen for electrons accelerated downwards as the frictions force will slow them down to a stop in the high density air.

These effects makes it possible for us to observe gamma-rays produced inside thunderclouds in detectors on satellites orbiting the earth as well as some energetic electrons that originate from high electric field regions inside thunderclouds. Gamma-rays can also be detected on the ground or in airborn detectors onboard airplanes or balloons. As the attenuation of the gamma-rays is dependent on distance and air density between the source and the detector, positioning of detectors relative to the source is of importance with regards to the quality of the measurements.

Chapter 3

Observations of gamma-ray glows

After Wilson's suggestion regarding very energetic electrons in conjunction with thunderstorms [*Wilson* (1925)], a number of experiments were conducted in order to look directly for the energetic electrons. The experiments were conducted in the period 1930s to 1960s with mixed results. Observations of high-energy x-ray radiation from thunderstorms began in the 1980s with airplane flights [*Parks et al.* (1981)] and later with balloons in the 1990s [*Eack et al.* (1996b)]. The observations were conducted in search of evidence to support the predictions made by *Wilson* (1925) that runaway electrons could be responsible for x-ray radiation from thunderclouds. In this chapter we will describe the observations that since then have been made and give a summary of which questions are left to be answered.

3.1 Airborne measurements

Parks described measurements from an X-ray detector that was flown on-board a NASA F-106 jet into thunderstorms [*Parks et al.* (1981)], they detected an increase of 3 times above background radiation levels. The NaI scintillation detectors carried resolved energies in three channels with the highest channel detecting energies above 12 keV. It was therefore at this time not evident that x-rays in thunderstorms extended to much higher energies. According to *Dwyer et al.* (2012) there were some evidence of anti correlation between lightning and the observed high-energy radiation in these first data, but it was not significant enough to overcome the natural presumption that the high-energy radiation was directly associated with lightning.

Later flights [*McCarthy and Parks* (1985)], carried detectors that had a energy range extending up to 110 keV. These flights demonstrated two important facts; (1) that the radiation extended to higher energies (>110 keV) and (2) that the radiation has longer time scales than that of a flash of lightning. The increase in radiation both varied smooth over tens of seconds, but also had rapid increases over short time spans and the higher energies extend to at least >110 keV. The paper also showed that lightning, either nearby or striking the plane, generally does terminate rather than cause the x-ray glows.

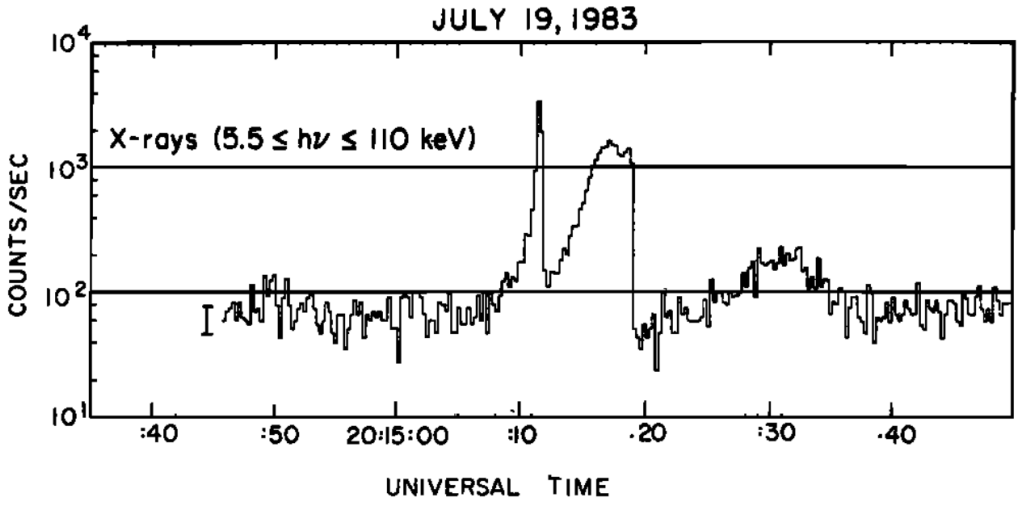

Figure 3.1: Three x-ray events from McCarthy and Parks (1985). The abrupt termination of the two first events coincided with a nearby lightning flash for the first one and a strike to plane for the second one. The third event has a gradual decrease. Figure from McCarthy and Parks (1985)

As can be seen in Figure3.1, the glows can have both a steep rise as in the first increase 80 times above background, from 20:15:10, or a gradual nature as in the second increase 30 times above background (20:15:12 - 20:15:20). At times 20:15:12 and 20:15:20 abrupt terminations of the radiation associated with lightning are seen. Later (20:15:20 - 20:15:40) a more gradual build-up of radiation can be seen with a gradual decrease that might be due to the aircraft with detector leaving the region of radiation production.

During the 1990's Eack and collaborators used balloons to carry both scintillators and electric field detectors. The instrumentation was carried with balloons through and above active cells [*Eack et al.* (1996b), *Eack et al.* (1996a), *Eack et al.* (2000)].

The first balloon flight as described in *Eack et al.* (1996a) produced measurements as shown in Figure 3.2, a hard x-ray glow with 250 times increase above background was measured at 4 km altitude coinciding with a peak in the electric field. The energy measured was between 30 and 120 keV, while the measured electric field was not close to the break-even field for 1 MeV runaway electrons. At 3.8 km the radiation and electric field measurements shows dips in the measurements that coincided with a pair of lightning flashes. The electric field measured by the balloon was assumed insufficient to produce the measured x-rays, while the field at the production site for the radiation could well be above the given value for break-even field as x-ray can travel through the atmosphere undergoing scattering, but still have energies and counts substantially above background levels of radiation. As the assumed production mechanism for these measurements were run away electrons it remains to evaluate the MOS process as a possible local production mechanism with the measured electrical field strength.

Another balloon flight the same year as described in *Eack et al.* (1996b) found shorter X-ray pulses after the balloon had penetrated the cloud top and was flying at 15km above mean sea level (MSL) (about 3km above the electrical cloud top). The measured radiation had a maximum value 100 times above background and they had

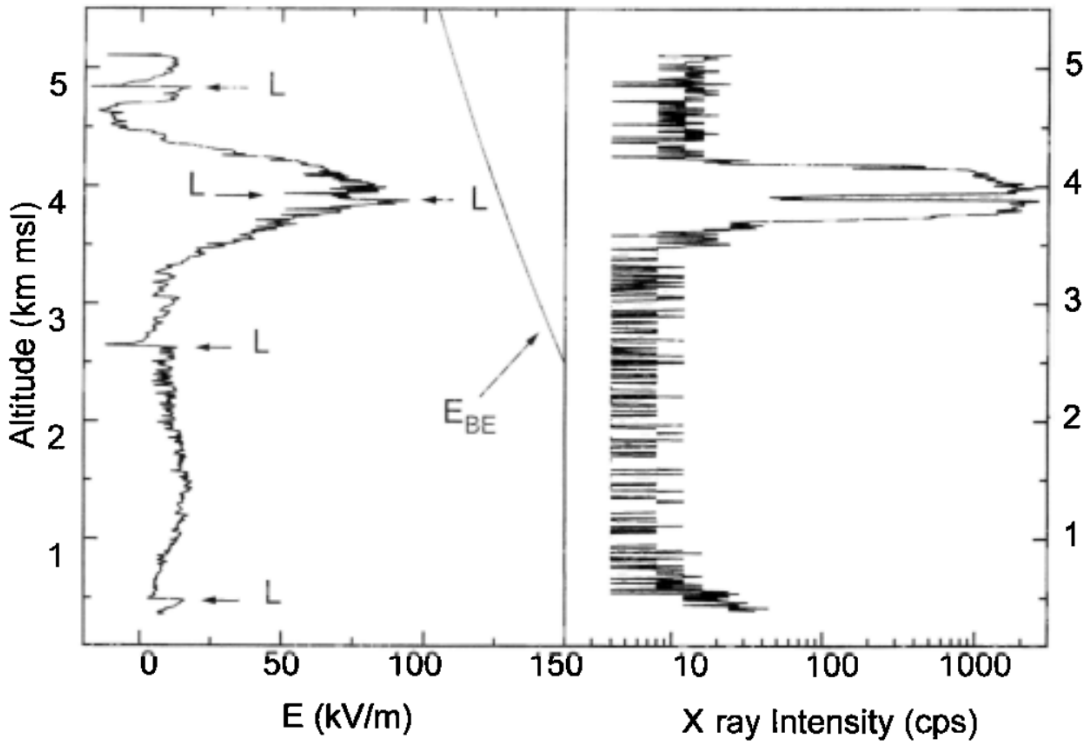

Figure 3.2: Balloon measurement of electric field and x-ray count rate. Lightning flashes are marked with "L" and predicted break-even field for 1 MeV runaway electrons is marked E_{BE} on the electric field panel. Figure from Eack et al. (1996a)

duration of about 1 second each. The balloon measured no significant electrical field at the time of the measured x-rays. The x-ray detector was limited to detect radiation from above, but the authors discussed the possibility of x-rays coming from production inside the thundercloud or from a high field region just above the storm that could be created temporarily by charge movements associated with a lightning flash. X-rays could propagate to above the balloon and Compton scatter downwards to the detector. In the case of the temporary high field region, the pulse time scale of seconds derives from the relaxation time, which is the time it takes for a screening layer to reassemble and cancel the quasi static field above the storm.

In 1998 another sounding as described by *Eack et al.* (2000) found no x-rays above background during the ascent of the balloon, but after the balloon burst and it was falling the x-ray instruments triggered on two high flux events in an anvil at 14 km. The measured radiation had a magnitude of 3 times the background level and lasted for an estimated 20 seconds. There was two triggers recorded with 10 s apart (10 s being approximately the x-ray instrument re-arm time), it is uncertain if the two triggers were from independent events or from the same x-ray production event. These measurements suggest that glow phenomenon can occur in different parts of the charge structure of a storm and that it is not uncommon.

In the summer of 2009, Airborne Detector for Energetic Lightning Emissions (ADELE) observed 12 gamma-ray glows. The instrumentation was flying on the National Center for Atmospheric Research (NCAR) Gulfstream V airplane [*Kelley* (2014)]. The de-

tector was designed according to experience from ground and satellite-based measurements and it included 5" diameter by 5" long plastic and NaI scintillators for gamma-ray sensitivity above 10 MeV. To determine whether the radiation was coming from above or below lead sheets were placed above and below some of the detectors. While only one TGF was observed, 12 glows were observed during 37 hours of flight passing over or near the tops of active cells. According to *Kelley* (2014) the observed glows had an increase above background of 10-100 times and varied in duration from 4 to 112 seconds. For all but the brightest one the duration was consistent with the motion of the airplane past a stationary RREA area. Of course it is difficult to determine if the duration measured is equal to the full duration of the glow as the detectors on the airplane can move out of the radiation region before termination. The study made by *Kelley* (2014) show more lightning activity preceding the glow than following it. Possible reasons for this is that glows suppress lighting or that glows can only form when lighting activity diminishes. It is noted that glows were seen 11 out of 49 times that the plane passed near active lightning cells. It might be that gamma ray glows last as long as the high electric field regions that produce them.

In January 2016 an Airbus A340 aircraft flew over Australia carrying the In-Flight Lightning Damage Assessment System (ILDAS). As reported in *Kochkin et al.* (2017) during flight at 12 km altitude a long duration gamma-ray emission was detected. The emission lasted for 20 s and its intensity was 20 times the background counts, about 6 minutes later another increase was observed that lasted for 30 s. The first glow appears to be abruptly terminated by lightning, but according to *Kochkin et al.* (2017) the x-ray flux started to decrease prior to the EM pulse. The authors speculate that the glow could have collapsed and initiated a lightning strike.

During spring 2017 an ER-2 aircraft campaign was undertaken over continental United States. The aircraft was equipped with instruments to detect optical signals, electric fields and gamma rays from lightning. Two gamma ray glow events were analyzed with measurements taken at 20 km altitude and as reported by *Østgaard et al.* (2019) the on-board directional electric field meters indicate that the glows occurred in conjunction with an inverted charge structure. The magnitude of increase above background for the glow was 6-45% with 15 s duration for the highest level followed by a sudden drop to 16% above background.

Table of airborne measurements

Table 3.1 is a summary of the measurements described in this section. The table contains the altitudes of the measurements, the relative increase of x-ray counts above background level in per cent and the energy range of the detector as well as the duration of the measured radiation. For the early flights by *Parks et al.* (1981) and *McCarthy and Parks* (1985) as well as the balloon flights of *Eack et al.* (1996b), *Eack et al.* (1996a) and *Eack et al.* (2000) the highest magnitude increase of radiation is given, but for the later measurements the full range of the measurements are stated.

The first flights in the 1980s as well as the flights described in *Kelley* (2014) did not include electric field measurements, while the balloon flights in the 1990s and the later

airplane flights did measure the electric field at the balloon/airplane.

Table 3.1: Airborn x-ray measurements

Paper	Altitude [km]	Increase a.b. [%]	Energy [keV]	Duration [s]
Parks et al. [1981]	4	200	3 - >12	18-20
McCarty and Parks [1985]	9	8.000	5.5-110	2-20
Eack et al. [1996a]	15	10.000	30-120	1
Eack et al. [1996b]	4	25.000	30-120	60
Eack et al. [2000]	14	200	60-300	20
Kelley et al. [2015]	14-15	900-10.000	50-5.000	4-112
Kochkin [2017]	12	200-2.000	100-10.000	20
Østgaard et al. [2019]	20	6-45	300-40.000	15

Previous modeling work

Following the airplane flights of *Parks et al.* (1981) and *McCarthy and Parks* (1985) a study was made by *McCarthy and Parks* (1992) to try to find the source of the radiation. Two possible sources of seed electrons were proposed and modeled, cosmic-ray secondary electrons and electrons from radionuclides. Cosmic ray electrons were found to be a factor of 8 and radionuclides a factor of 300 too scarce too explain the observed radiation. However it was stated that the model was not accurate enough to rule out cosmic ray electrons as seed particles for the observed radiation.

The balloon flight from *Eack et al.* (1996a) was modelled by *Gurevich and Milikh* (1999). In their modeling work they used an RREA model and found good agreement with the observations. They estimated the distance between detector and source region to be 400 m and the thickness of the charge layer to be 240 m.

In the paper *Chilingarian et al.* (2014), the authors compared measured and modeled results for TGE radiation. the measurements are made at a experimental facility close to Mt. Aragats in Armenia. The author describes the MOS process and how this process produces a rather stable enhancement in the background flux between 1-100 MeV. The conclusion of the paper was that modest electric fields, below RREA threshold, initiate the majority of TGEs by the MOS process.

Following the ER-2 airplane campaign in the spring of 2017, *Østgaard et al.* (2019) described two possible production mechanisms MOS and RREA for the measured gamma ray glows. The two mechanisms were investigated by modeling in Geometry and tracking 4 (GEANT4) and they point out that the MOS mechanism can enhance the flux locally (on top of the cloud), while RREA can enhance the flux sufficiently inside the cloud in order to overcome the attenuation between production region and detector. Their simulations showed that the results could be produced by both upward and downward fields, but the estimated field strength at production altitude was a factor of 10 to small. For the RREA mechanism they

found that assuming a regular charge structure (not reversed as indicated by electric field measurements), the field strength has to be 1.2 times larger than the local RREA threshold inside the cloud. This result is based on the speculation that there could be some localized area where the charge structure was of the regular type.

3.2 Summary of observations

From early air born observations in the 1980s and on-wards the field of high energy atmospheric physics has blossomed and better technology has made the study of details related to gamma ray glows possible. Since the balloon flights of *Eack et al.* (1996a) which detected radiation at 4 km altitude our curiosity for knowledge regarding the exact mechanisms behind production of the radiation has not been sated. The exact mechanisms and field strengths responsible for the x-ray radiation from thunderclouds have not been determined. As of now there are two possible mechanisms that are being examined, RREA and MOS. The most likely source of seed particles is cosmic ray electrons and positrons. *McCarthy and Parks* (1992) showed that radionuclides are to scarce to account for increase in x-ray radiation and gamma-ray glows are generally thought to be terminated by lightning [*McCarthy and Parks* (1985)]. The mechanisms behind glow termination by lightning or perhaps gamma-ray glows initiating lightning [*Kochkin et al.* (2017)] is not known and one can speculate as to the role of the electrical field strength in this interplay.

The impossibility of measuring the electric field at the source location means we have to make assumptions in order to model the electric field value. While the balloon flights of *Eack et al.* (1996b), *Eack et al.* (1996a) and *Eack et al.* (2000) had field measurements inside the clouds it is still unknown how the electric field varies in horizontal direction inside the thundercloud. The model of the RREA mechanism have been further developed since *Gurevich and Milikh* (1999), last by *Dwyer* (2003). This means that it is relevant to revisit the earlier measurements with new modelling tools in order to revise the conclusions that previously were made. It is also interesting to explore models for the different measurements that take into account different vertical and horizontal distances between production region and measurement. The measured electric fields at a different distance in vertical and horizontal distance might give different x-ray production than the field measured at the balloon. The characteristic of the x-ray detectors should also be taken into account such that the modeling result become as realistic as possible.

Chapter 4

Monte carlo models

In this thesis two Monte Carlo (MC) models have been used: Particle and Heavy Ion Transport (PHITS) and GEANT4. Simulation results from PHITS are given in the PHITS-based Analytical Radiation Model in the Atmosphere (PARMA) database have been used as input to GEANT4 simulations. The relevant data from PARMA are the differential energy distributions of relevant particles (protons, electrons, positrons and photons), as a function of altitude and incoming angles.

One of the earlier uses of MC methods were simulations during the development of the atomic bomb in the Manhattan Project in the 1940s. MC simulations rely on repeated random sampling in order to provide generally approximate solutions. These techniques are used in cases where analytical or numerical solutions do not exist or are too difficult to implement.

In this project modeling work for propagation of the initial particle distributions through the atmosphere and electric fields has been preformed using GEANT4 simulation toolkit (set of software libraries and tools), where the initial particle distributions at a selected altitude are given by PARMA data. The reason for choosing this approach is to save computation and modeling effort as the input to our model can be taken at an altitude closer to the thundercloud electric field such that the full propagation of cosmic ray particles from outside of the atmosphere does not need to be computed.

In this chapter the two MC models, PHITS and GEANT4 are given a brief description.

4.1 PHITS

PHITS is a general purpose MC particle transport simulation code used in studies in the fields of accelerator technology, radiotherapy, space radiation etc. PHITS has been utilized in order to create the PARMA database. PARMA is a database with data based on MC simulations for extensive air showers (EAS) of cosmic ray particles in the atmosphere. In order for the reader to understand where the input data to our simulations originate this section will give a brief description of how the PARMA database has been constructed.

It requires considerable resources to reproduce PHITS simulation results [*Sato* (2015)], therefore analytical models that can give instantaneous estimates of the results were con-

structed. The models compromises theoretical and empirical equations with free parameters that are determined using least squares (LSQ) fitting of the MC simulation results. For this project it was decided that the energy, number and angular distributions of cosmic ray initial distribution particles should be based on this database. The version of the database used in this project is version 4.0. In this thesis we refer to PARMA for the database and PHITS for the simulation.

PARMA has according to *Sato* (2016) been developed since 2006, in the beginning for neutrons at altitude below 20 km for calculation of radiation doses for aircrew. The model has been continuously updated to include more of the secondary particle species that are produced during cosmic ray showers as well as particles of altitudes up to 63 km [*Sato* (2015)].

For the PHITS simulations the source particles were galactic cosmic rays (GCR) protons and ions with energies up to 1 tera electron-volt per nucleon (TeV/n) and the heaviest ion nickel (Z=28). GCR fluxes were calculated using a model proposed by *Matthiä et al.* (2013). As described by *Sato* (2015) fluxes were calculated at 1 astronomical unit (AU) for particle type i, with energy E, for sunspot number W. The fluxes $\varphi_{i,1AU}(E,W)$, can be calculated by Equation 4.1. According to *Matthiä et al.* (2013) the value for W used in Equation 4.1 differs from the wulf number. The reason for this is a need to fit the model to experimental data and a full explanation can be found in *Matthiä et al.* (2013).

$$\varphi_{i,1AU}(E,W) = \frac{a_{1,i}\beta^{a2,i}}{R(E)^{a3,i}}\left\{\frac{R(E)}{R(E)+[0.37+0.0003W]^{1.45}}\right\}^{a_4W+a_5}\frac{A_i}{|Z_i|}\frac{1}{\beta} \tag{4.1}$$

Where A_i and Z_i are the mass and charge numbers of the particles respectively, R(E) is the rigidity of the particle in giga-volt (GV), and β is the speed of the particle relative to light. Parameters $a_{1,i}$ - $a_{3,i}$ are free parameters depending on particle type i, while a4 and a5 are constant for all particles.

The simulations were conducted using PHITS version 2.73 for solar minimum W=0 and near maximum conditions W=150 and for 21 geomagnetic field locations with R_C ranging from 0 to 20 GV. In the simulation, all particles were traced down to 10 keV, with the exception of neutrons, which were transported down to 0.01 eV. The angular distribution of particles crossing 18 surfaces at altitudes of between 0 and 52 km were recorded as a function of $cos(\theta)$, where θ is the zenith angle to the downward direction. The atmosphere was modeled as 28 concentric shells with maximum altitude 86 km and with densities according to the US Standard Atmosphere 1976. Cosmic rays were incident from the top of the atmosphere in the isotropic irradiation geometry. The atmosphere above 86 km was not taken into account for these simulations due to the low density in that region which means it is assumed to have a minimal effect on the incident cosmic rays.

PARMA contains energy spectrum for particles of type: protons, helium-ions, neutrons, electron, positrons, photons, positive muons and negative muons as well as the angular fluxes for these particle types. The unit of the output flux is either for the omnidirectional differential flux given in Equation 4.2 or for the directional differential flux given in Equation 4.3. Input parameters include: atmospheric depth d in g/cm^2, altitude or pressure. Vertical cut-off rigidity R_c in GV or Latitude. Solar modulation index W or date. The fluxes are given for an energy range $10^{-2} - 10^6$ MeV and the energy is stated per nucleon where n is the number of nucleons.

$$\frac{1}{cm^2\, s\, (MeV/n)} \tag{4.2}$$

$$\frac{1}{cm^2\, s\, (MeV/n)\, sr} \tag{4.3}$$

There are some discrepancies between PARMA and PHITS simulation data for neutrons, electrons and positrons with energies over 5 GeV between 0 and 11 km altitude. However according to *Sato* (2016) PARMA allows for instantaneous estimation of the differential cosmic-ray fluxes under most practical situations with an accuracy equivalent to that of the EAS simulation. Further *Sato* (2016) also states that PARMA has satisfactory accuracy compared with multiple sets of experimental data. The PARMA data for muons and protons have particularly good agreement with experimental data except for high energy data near sea level. It is also noted that the PARMA database overestimates high-energy electron fluxes and underestimates the lower altitude photon fluxes [*Sato* (2016)].

4.2 GEANT4

GEANT4 is a toolkit written in C++ for the simulation of the passage of particles through matter [*CERN*]. Areas of application for the toolkit include high energy, nuclear and accelerator physics, as well as studies in medical and space science. The GEANT4 toolkit uses the MC method in order to simulate particle interactions.

The length before interaction is expected to take place is determined by evaluation of all applicable processes for each step. If the particle mean free path ends inside the given volume it will interact otherwise it will cross the boundary to the next volume before the interaction potentially takes place. The trajectory of particles is determined by boundary crossings, effects of external fields, scattering processes and transportation processes.

Particle transport in GEANT4 is determined by calculation of mean free path of the different processes. The mean free path or interaction length is then given by the total cross section summed for all physical processes and all the elements of the medium the particle is being propagated through. The trajectory of particles in external fields is determined by splitting the trajectory into chord segments that are numerically calculated.

The cross sections for each interaction process are based on experimental data and model calculations. Especially relevant for the work in this thesis are the; photon processes: photo electric effect, Compton scattering and pair production; electron and positron process: Bremsstrahlung. Also relevant for the simulation of proton transport is the energy loss by ionization, decay processes and hadronic processes that are relevant for the hadronic showers when cosmic rays interact with the earths atmosphere.

Chapter 5

Methodology

In this chapter we will describe the methodology behind our simulations of cosmic-ray particles propagating in the atmosphere. The description contains all the assumptions and simplifications that has been implemented in order to create our simulation environment.

5.1 GEANT4 - implementation

In this section we describe how we use the two MC models, how the output from PARMA is used as input for GEANT4 and how we test the compatibility between the two codes. We also describe how we implement the atmosphere and electric field in GEANT4, as well as the type of particles and their energy ranges.

5.1.1 Atmosphere

The spherical geometry of the atmosphere has been simplified as a cylinder with diameter 100 km and height from 0 to 50 km above mean sea level. This allows for initial particle distribution to be entered at a selected height in a horizontal plane parallel and offset from the xy-plane intersecting the origin. The recording of particles crossing through different altitudes can similarly be done by testing which particles cross a horizontal plane also parallel to the xy-plane intersecting the origin for a selected number of altitudes.

The diameter of the cylindrical simulation environment was chosen in order to be able to input particles from the origin at 50 km altitude of up to 45° zenith angle, while avoiding the particle crossing the cylinder boundary before reaching 0 km altitude (assuming no particle interactions). The process of input particle distributions is further explained in Subsection 5.1.4 and the maximum zenith angle is visualized in Figure 5.4. The diameter is calculated according to Equation 5.1, where Δh is the height difference, and θ is the zenith angle.

$$D = 2(\frac{\Delta h}{tan(\theta)}) = 2(\frac{50\,km}{tan(45°)}) = 100\,km \tag{5.1}$$

The atmosphere data used by the model is calculated based on the reference atmospheric depth data as given by the PARMA database, this data is the yearly average of NRLMSISE-00.

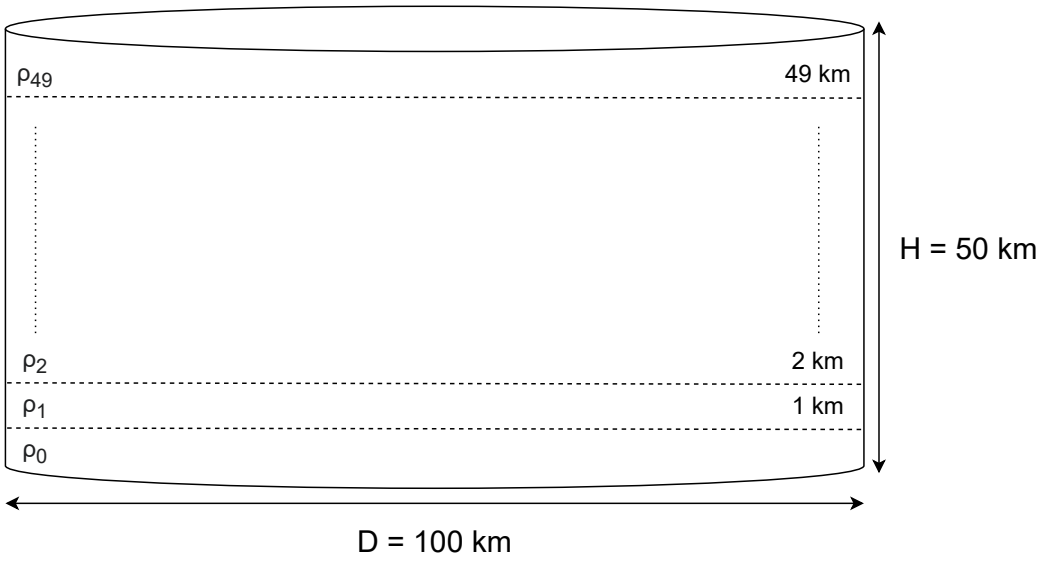

Figure 5.1: Simulation geometry with implementation of atmospheric density in steps of 1 km in the GEANT 4 model.

The atmospheric depth data given in steps of 1 km has been converted to average atmospheric density pr. step by Equation 5.2.

$$\rho_i = \frac{Da_i - Da_{i+1}}{h} \tag{5.2}$$

Where Da_i is the atmospheric depth at vertical position i and Da_{i+1} is the atmospheric depth at vertical position i+1, i is the step number and h is the step length. The units of atmospheric depth is: $\frac{g}{cm^2}$ and the units of atmospheric density is: $\frac{g}{cm^3}$. Atmospheric depth is the integral of the atmospheric density from the top of the atmosphere and down to a given altitude, therefore the average density between two altitudes can be found by taking the average of the atmospheric depth between two altitudes and dividing by the altitude difference. The implementation of the atmosphere is sketched in Figure 5.1.

A comparison has been made between the calculated density based on data from the PARMA database and density data from the NRLMSISE-00 atmosphere model for location Longyearbyen with coordinates 78°N and 16°E. The comparison is made for NRLMSISE-00 for months: january, april, july and october. The results of comparison have been visualized in Figure 5.2 and Figure 5.3 where the graphed relative difference is the absolute difference between the values from the PARMA and MSISE dataset divided by the value from the PARMA database and given in per cent.

5.1.2 Electric field

GEANT4 has the capability of describing the propagation of particles in many different forms of fields. Magnetic Fields, electric fields and gravitational fields both uniform and non-uniform. In this thesis the field in question is the electric fields that are associated with thunderstorms which is known to accelerate electrons and positrons to energies where they can produce photons by bremsstrahlung.

The modeled electric field is uniform and has adjustable strength and size. The field spans

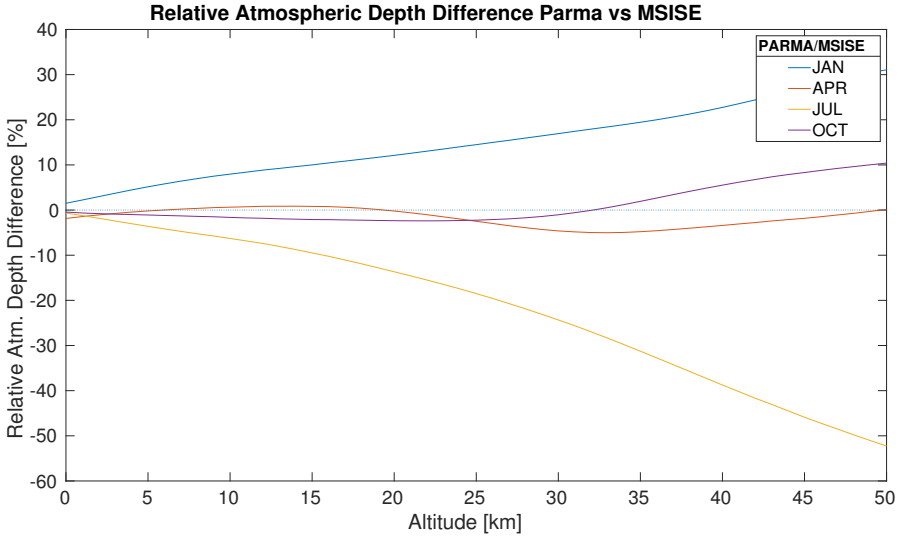

Figure 5.2: Relative ratio of difference between atmospheric depth from MSISE and PARMA.

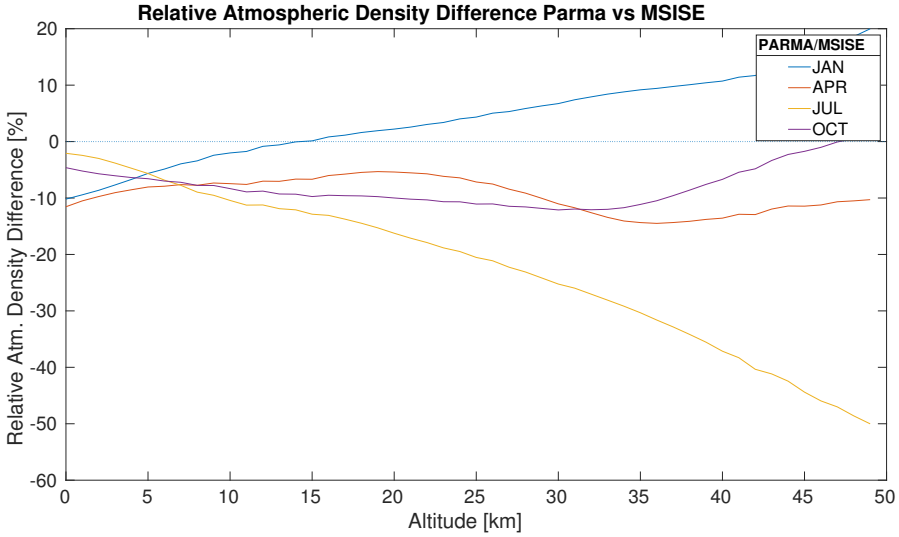

Figure 5.3: Relative ratio of difference between atmospheric density from MSISE and PARMA.

the entire xy-plane between selected altitudes. The choice of uniform electric field is a simplification that is done in order to be able to model the MOS and RREA processes for a typical simplified three pole charge structure as described in Subsection 2.1.2. The mechanisms behind thundercloud electrification are complex and locally higher field values will occur inside of a thunderclouds. However it is important to emphasize that in order to study a large scale phenomenon certain assumptions have to be made in order to be able to study the overall effects. Therefore the field is kept constant over a defined height segment in this thesis.

5.1.3 Particles included in the simulation

GEANT4 can use several physics list, adapted for different contexts. The physics list is used to instantiate particle types and interaction processes for the simulations and different lists will have better accuracy for specific applications. GEANT4 separates the physics list into two separate components where the hadronic physics relevant for protons in our simulations and the electromagnetic physics relevant for photons, electrons and positrons are separated. Based on the recommendations from *Geant4 Collaboration* (2017) the QBBC list for the hadronic component was chosen as this list is recommended for space physics simulations.

The QBBC physics list uses a GEANT4 default electromagnetic physics list. Adaptations to the electromagnetic physics list is relevant when running MC simulations with a large particle count. This is relevant for gamma-ray glow simulations where the computational time can be reduced with an acceptable sacrifice to the accuracy of the simulation.

The energy range for the particles is constrained to the energy given by the PARMA database with range 10^{-2} - 10^{6} MeV.

5.1.4 Initial particle distribution from PARMA

The process of recreating the initial particle distribution from the PARMA database is done based on random numbers that select the zenith angle and sampling of particle energy from energy distributions. The energy distributions are given for 0°, 10°, 20°, 30° and 40° zenith angle. Zenith angle is chosen as either 0°, 10°, 20°, 30° or 40° based on a weighting of the integrated fluxes for the energy distributions for these angles. The zenith angle as described in the PARMA documentation is the nadir angle where 0° corresponds to vertical down, in this thesis zenith angle will follow the same definition to avoid confusion with regards to PARMA data.

All particles are entered into the simulation at the origin (X=0 and Y=0) at Z km altitude, where Z is selectable dependent on simulation setup. The zenith angle between 0-40° defines the relative vectors of initial propagation by Equation 5.3, where ϕ is the zenith angle and θ is the azimuth angle (θ is randomly selected 0-360°).

$$X_{dir} = sin(\phi)cos(\theta) \qquad Y_{dir} = sin(\phi)sin(\theta) \qquad Z_{dir} = -cos(\phi) \tag{5.3}$$

By running this procedure for sampling primary particles with a satisfactory number of particle counts the goal is to recreate the distribution of particle species, angles and energies as given by the PARMA database for the selected input sampling altitude. The satisfactory number

of particles is dependent on what the experiment aims to recreate. As one wants to avoid statistical fluctuations, it is imperative to evaluate the intended input energy distribution for distribution of probabilities so that the particle count is high enough to represent the energies of interest. If there are energies in the selected distribution that have a high impact on the result, but a low probability of sampling, care must be given. It might be required to run a very high count of sample particles or to split the distribution up into regions, simulate them separately and normalize before combination of results.

5.1.5 Particle detection

In order to detect different particle species at different altitudes there were defined several detection altitudes where they were recorded to file. The detection included recording of all particles crossing the surface of the plane of that altitude. The detector writes the recorded particle type, energy, position in x, y, z-directions, momentum in x, y, z-directions as well as the time since the specific particle entered the simulation.

The same procedure is used to record the input particles that are recreating the initial energy distributions. For these particles the altitude of initial particle distribution, particle type and particle energy are recorded.

5.2 Simulation setup

There are two distinct simulation setups in this thesis. The first for reproduction of the energy distribution of protons from 50 - 10 km altitude. The second setup for reproduction of electron, positron and gamma-ray distributions from 20 km and down to thunder cloud altitudes, as well as changes to these distributions when electric fields are included. The second setup is referred to as glow simulation setup.

5.2.1 Testing compatibility between PARMA and GEANT4 for protons

This simulation setup is made in order to simulate the propagation of protons between the altitudes of 50 - 10 km and in order to compare the fluxes at lower altitudes with the PARMA data. Our simulation does not contain a magnetic field and in order to avoid discrepancies due to lack of magnetic deflection the simulation is set to a location where R_c is zero in the PARMA initial particle distribution data. The solar activity is set to W = 100, corresponding to medium/high solar activity. The setup is visualized in Figure 5.4.

For a representation of the input particle distributions a sampling test was conducted. Testing yields that particles with energy lower than 10^2 Mev has a minimal effect on distribution at lower altitudes, therefore the input particle distribution is sampled in the energy range 10^2 - 10^6 MeV. Further the relative abundance of particles in the energy range 10^2 - 10^4 MeV makes it infeasible to sample the complete distribution without increasing the sampling particle count to an unreasonable number. Therefore the distribution is split into three parts that are sampled

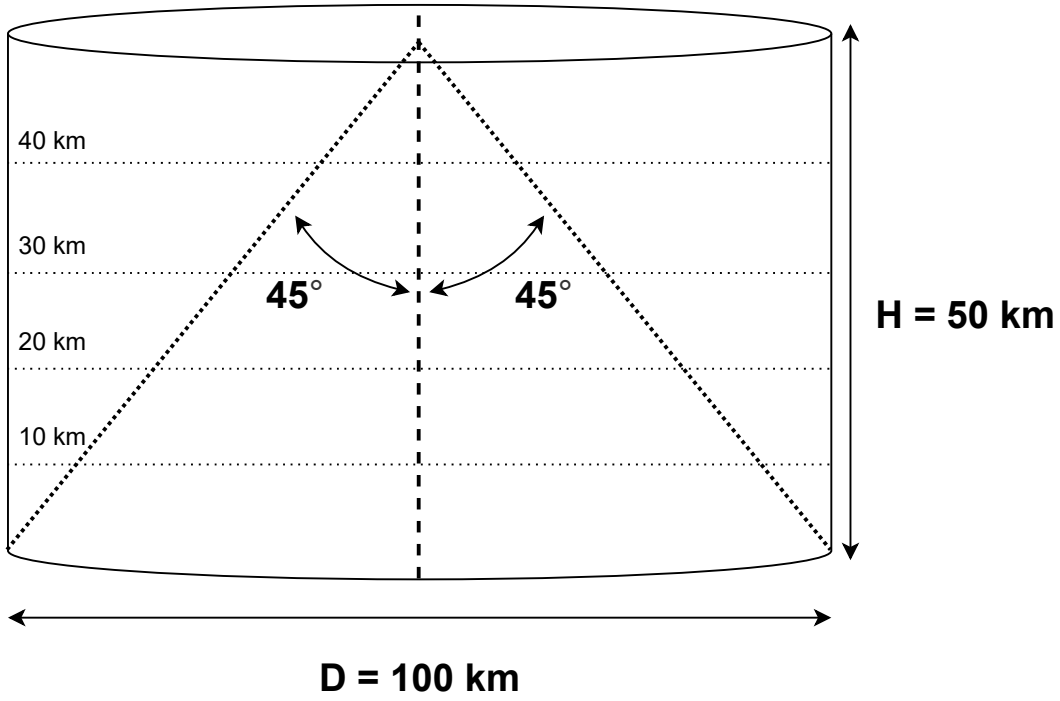

Figure 5.4: Simulation geometry protons. Recording surfaces are visualized as dotted lines and maximum sampling angle ϕ is visualized.

separately where the results from each sampling is weighted together. The energy ranges sampled are ordered in Table 5.1 and the minimum number of sampling particles per sample is 20.000 for representation of the complete energy spectra.

Table 5.1: Proton sampling energy ranges

Sample	Lower Energy [MeV]	Higher Energy [MeV]
1.	10^2	10^4
2.	10^4	10^5
3.	10^5	10^6

The particles are recorded passing planes with altitudes of 40, 30, 20 and 10 km. From the recorded data both the number of particles, their energy and the angles by which they cross the recording plane are stored.

5.2.2 Glow simulation setup

This simulation setup is made in order to simulate the propagation of electrons, positrons and photons between the altitudes of 20 km and thundercloud altitudes. The intention of the simulation is to reproduce the energy distribution of these particles with and without an electric field. The simulation setup is visualized in Figure 5.5.

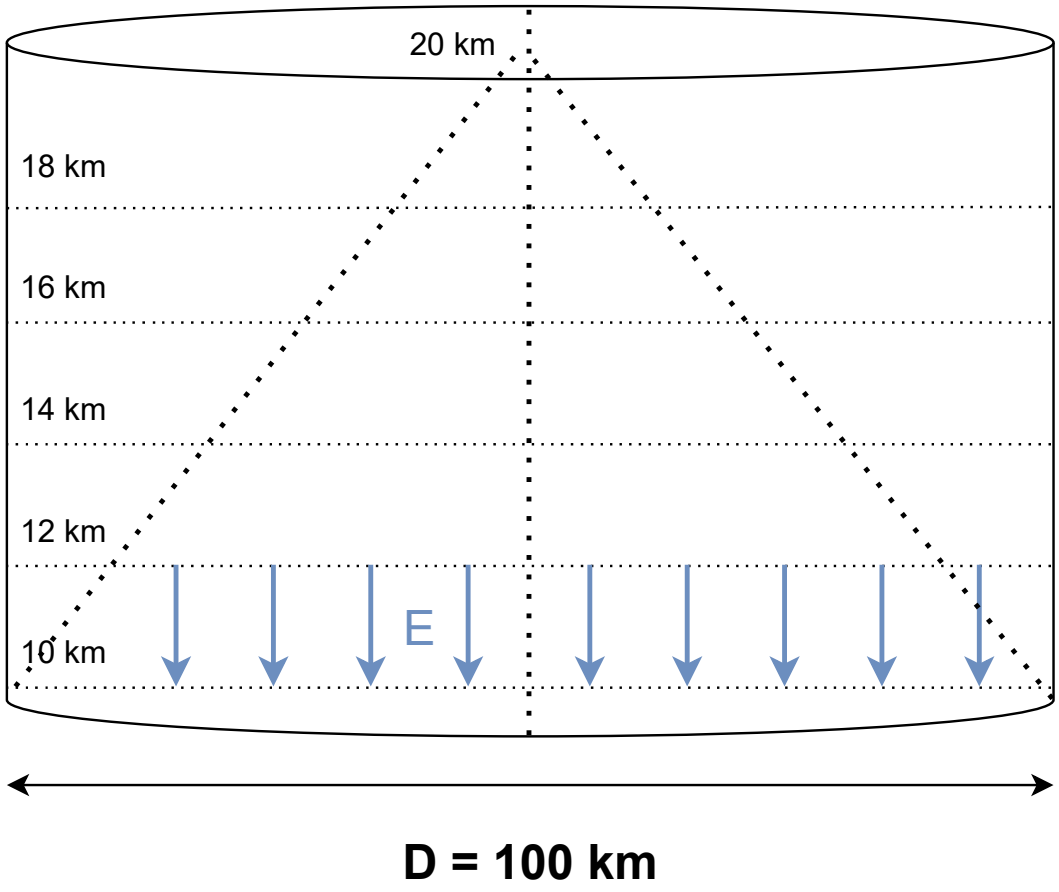

Figure 5.5: Glow simulation geometry. Surfaces for recording are visualized as dotted lines and electrical field with blue lines. Note: scale for x- and y- directions are independent.

Detection of particles is for this setup configured to detect particles passing planes at altitudes of 18, 16, 14, 12 and 10 km. From the recorded data both the number of particles, their energy and the angles by which they cross the recording plane is stored.

To test the effect of accelerating/retarding charged particles in the electric field a uniform field is modeled between altitudes 10 - 12 km. The field is modeled with the electrical field vector pointing downwards from the main positive charge region of the thundercloud to the main negative charge region. The field strength is adjustable between 0 and -80 kV/m in steps of 10 kV/m where recordings of the flux of photons, electrons and positrons are made at 12 km altitude. The goal is to simulate the production processes for gamma-ray glows: MOS and RREA. We also want to observe the transition in between glow production processes as the field is gradually increased and the change to the energy spectrum of photons.

5.3 Glow scenarios

The goal of this section is to make outlines of how to model simulation setups for the measurement results from Chapter 3. These measurement results were summarized in Table 3.1 and previous modeling work to reproduce them was summarized in Section 3.1. The understanding of the phenomenon of gamma-ray glows and the production processes responsible for them has increased substantially since the 1980s when x-ray radiation in conjunction with thunderclouds was first recorded. This means that we have the opportunity to revisit the already completed modeling work and check if newer tools and new ideas can help explain the production processes better.

I will here discuss how the balloon measurements described in *Eack et al.* (1996a) can be modeled for further investigation of the production mechanism behind the measured radiation. As described in *Eack et al.* (1996a) the balloon E-field meter and the x-ray counter peaks around the same time and has a disturbance due to lightning in the middle of the peak. The field as measured at the balloon is too low according to the calculated E_{BE} value for the altitude and the measurement results can therefore not be explained directly by the measured field, assuming that the runaway electron hypothesis is responsible for the observed radiation. However the MOS mechanism can still be responsible and should be tested at the observed field strength. Further the balloon might not be flying through the region of x-ray production, the task of recreating the x-ray flux by modeling therefore becomes a task of finding the most likely production location of the x-rays and modeling conditions at the location to match the needed x-ray production for the flux at the measurement location to become comparable to the measured values. Since the measurements are conducted at relatively low altitudes with a positive electric field value and an assumed lower seed electron population than at higher altitudes it is of interest to look at how x-ray produced at higher altitudes might propagate down to the balloon and cause the measured values. Another possible explanation might be that the electric field of the production region lies in the same altitude but in another horizontal location. By modifying electric field parameters and distance from detector it is possible to test both these two hypothesises.

Chapter 6

Results

This chapter describes the results of MC simulations with GEANT4 using PARMA data as input. The results is shown as a comparison between PARMA database and the results from GEANT4 simulations.

6.1 Transport of protons - comparison of codes

The purpose of this comparison is to test the compatibility between PARMA and GEANT4 and identify differences in the simulation results from GEANT4 and the PARMA database at altitudes 40, 30, 20 and 10 km above mean sea level. The data is displayed as energy distributions in order to both compare the energy distributions as described by distributions from PARMA and from the GEANT4 simulations. The simulations were conducted in parts for three different energy ranges as described in Subsection 5.2.1.

For comparing the energy distribution from the two codes, we will present normalized spectra from the two codes at altitudes 50 km, 40 km, 30km, 20 km and 10 km. For each altitude we show 5 different angular bins (see Table 6.1). This was done by sampling the momentum direction as the particles cross the recording surfaces.

Table 6.1: Angular bins

Angle (°)	Lower bound (°)	Upper bound (°)
0	0	5
10	5	15
20	15	25
30	25	35
40	35	45

The energy distributions are plotted between energies $10^2 - 10^6$ MeV with 40 logarithmic bins. In each figure the y-axis corresponds to the number of particles per bin and the x-axis

represents particle energy. The 50 km altitude distributions are included to document the initial particle distribution in the GEANT4 simulation.

6.1.1 Comparison at 50 km

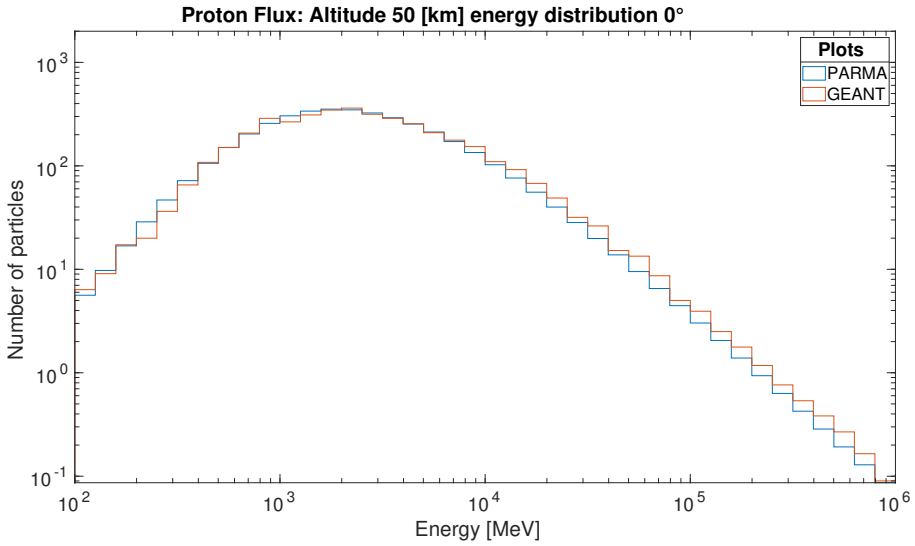

Figure 6.1: Energy spectra for PARMA and GEANT4 simulation at 50 km altitude above MSL and 0° zenith angle. The blue histogram corresponds to PARMA and the red histrogram to simulation results from GEANT4.

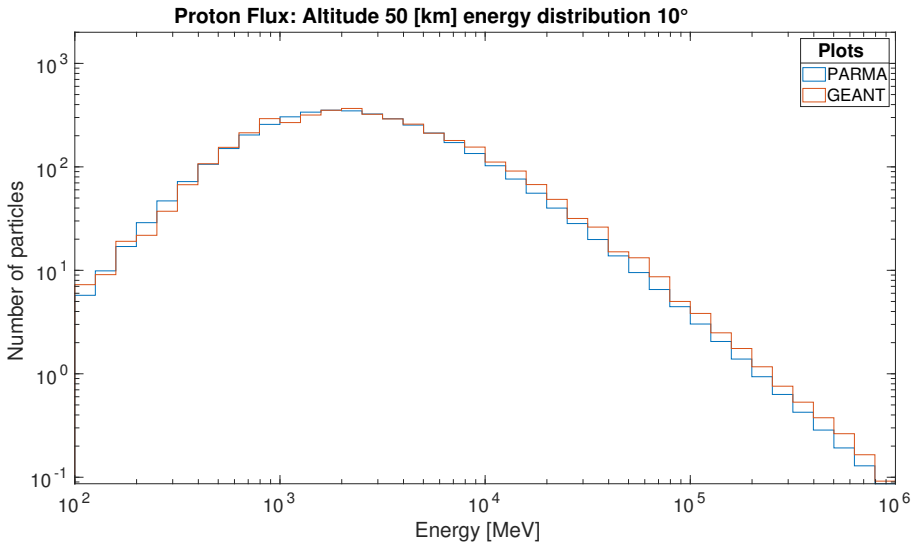

Figure 6.2: Energy spectra for PARMA and GEANT4 simulation at 50 km altitude above MSL and 10° zenith angle. The blue histogram corresponds to PARMA and the red histrogram to simulation results from GEANT4.

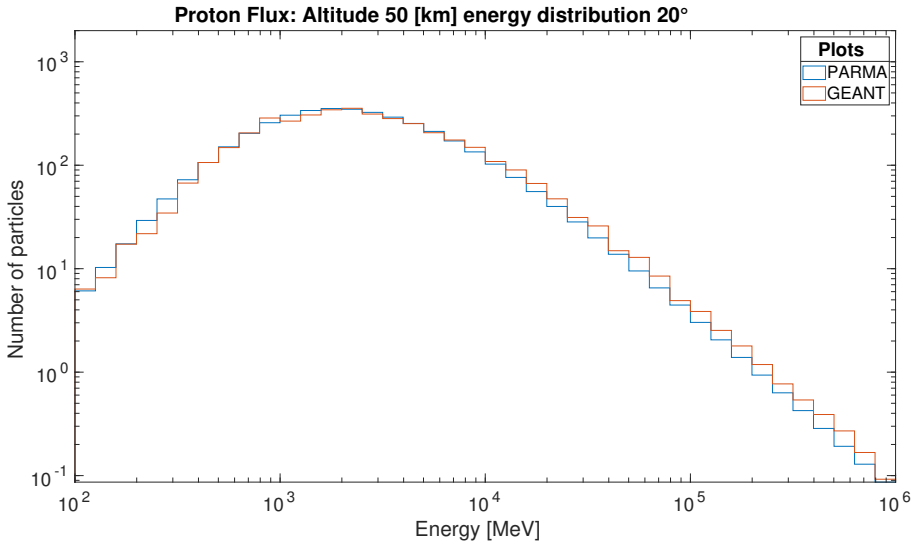

Figure 6.3: Energy spectra for PARMA and GEANT4 simulation at 50 km altitude above MSL and 20° zenith angle. The blue histogram corresponds to PARMA and the red histrogram to simulation results from GEANT4.

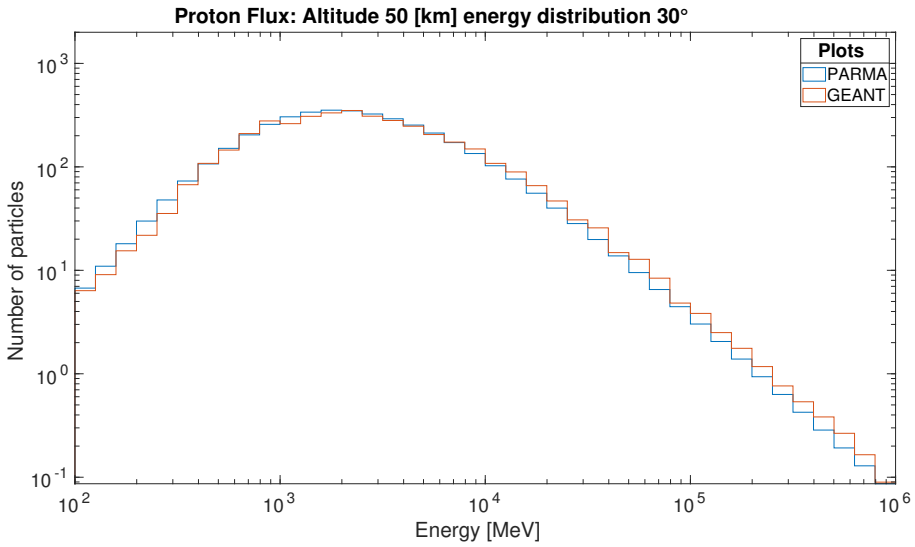

Figure 6.4: Energy spectra for PARMA and GEANT4 simulation at 50 km altitude above MSL and 30° zenith angle. The blue histogram corresponds to PARMA and the red histrogram to simulation results from GEANT4.

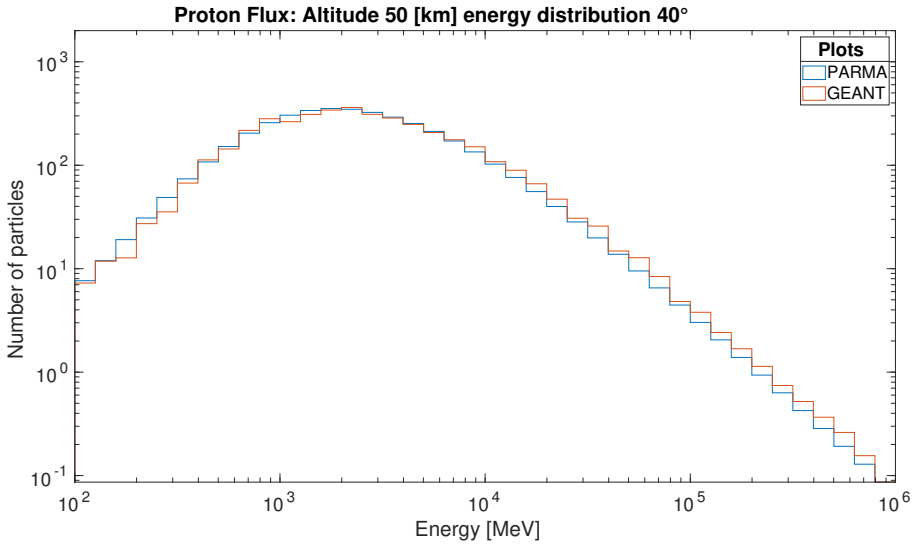

Figure 6.5: Energy spectra for PARMA and GEANT4 simulation at 50 km altitude above MSL and 40° zenith angle. The blue histogram corresponds to PARMA and the red histrogram to simulation results from GEANT4.

6.1.2 Comparison at 40 km

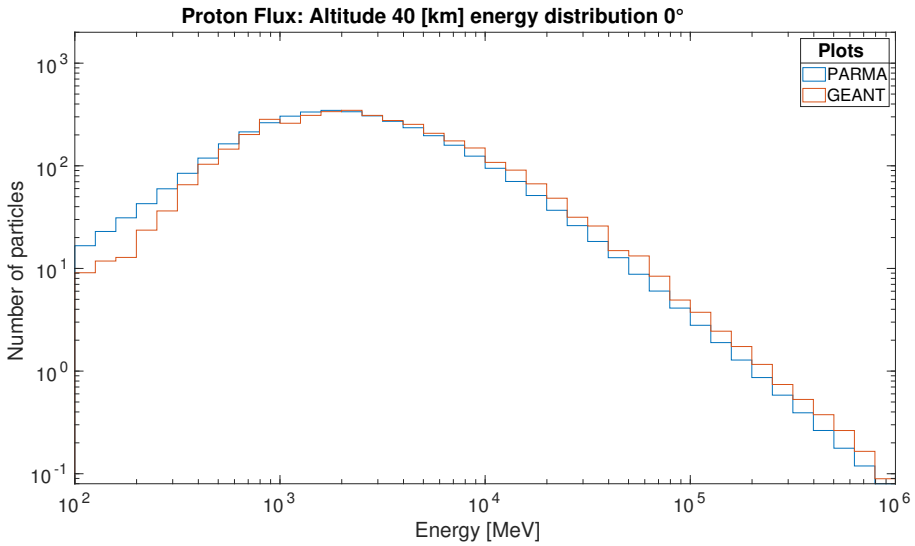

Figure 6.6: Energy spectra for PARMA and GEANT4 simulation at 40 km altitude above MSL and 0° zenith angle. The blue histogram corresponds to PARMA and the red histrogram to simulation results from GEANT4.

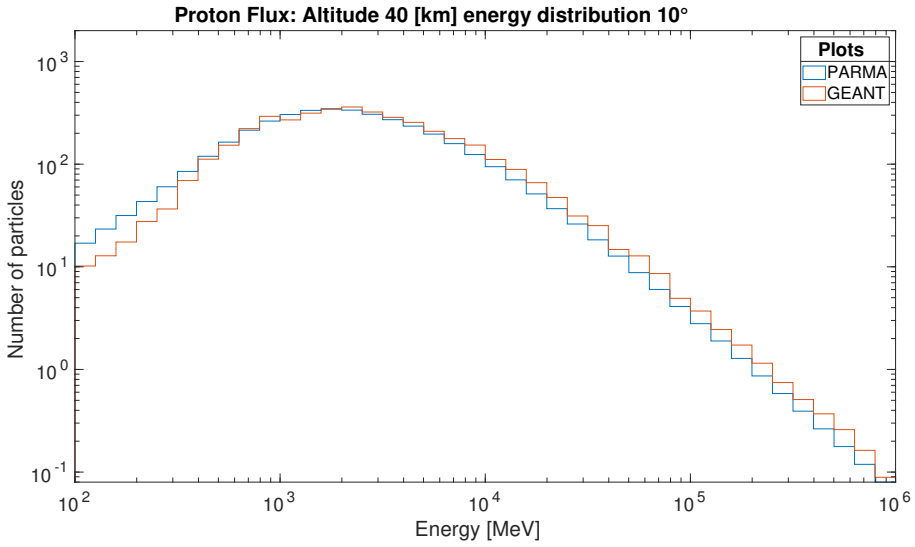

Figure 6.7: Energy spectra for PARMA and GEANT4 simulation at 40 km altitude above MSL and 10° zenith angle. The blue histogram corresponds to PARMA and the red histrogram to simulation results from GEANT4.

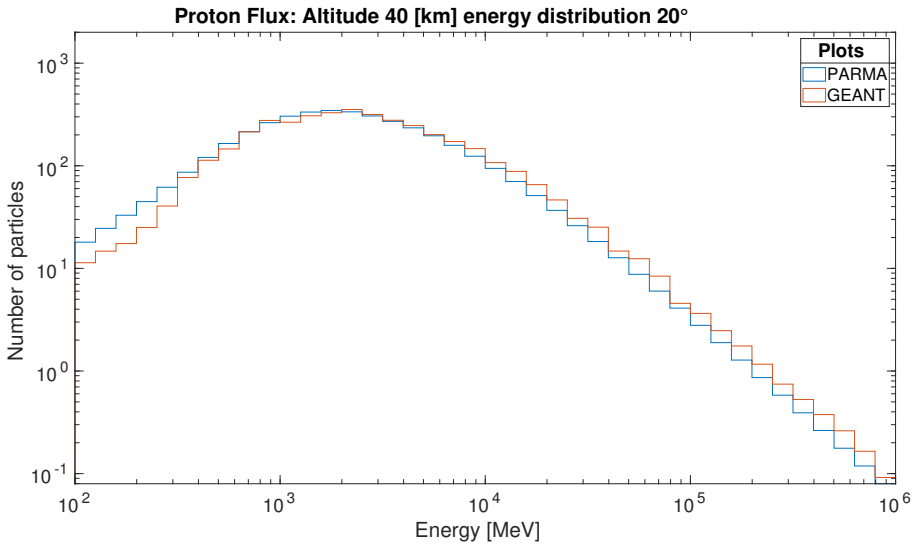

Figure 6.8: Energy spectra for PARMA and GEANT4 simulation at 40 km altitude above MSL and 20° zenith angle. The blue histogram corresponds to PARMA and the red histrogram to simulation results from GEANT4.

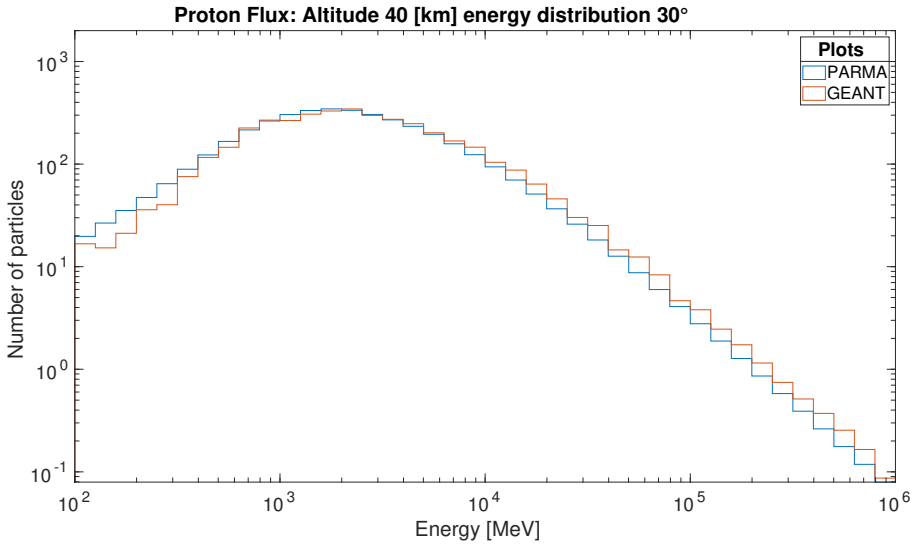

Figure 6.9: Energy spectra for PARMA and GEANT4 simulation at 40 km altitude above MSL and 30° zenith angle. The blue histogram corresponds to PARMA and the red histrogram to simulation results from GEANT4.

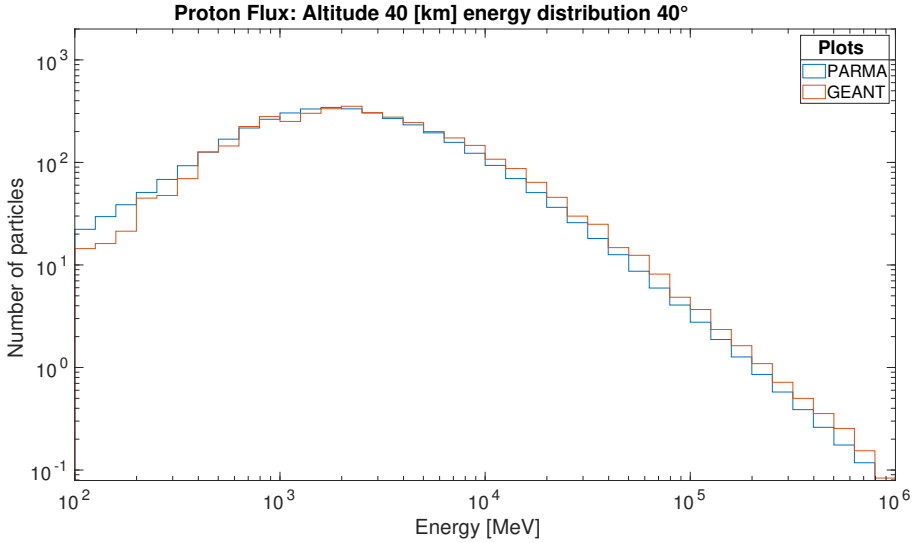

Figure 6.10: Energy spectra for PARMA and GEANT4 simulation at 40 km altitude above MSL and 40° zenith angle. The blue histogram corresponds to PARMA and the red histrogram to simulation results from GEANT4.

6.1.3 Comparison at 30 km

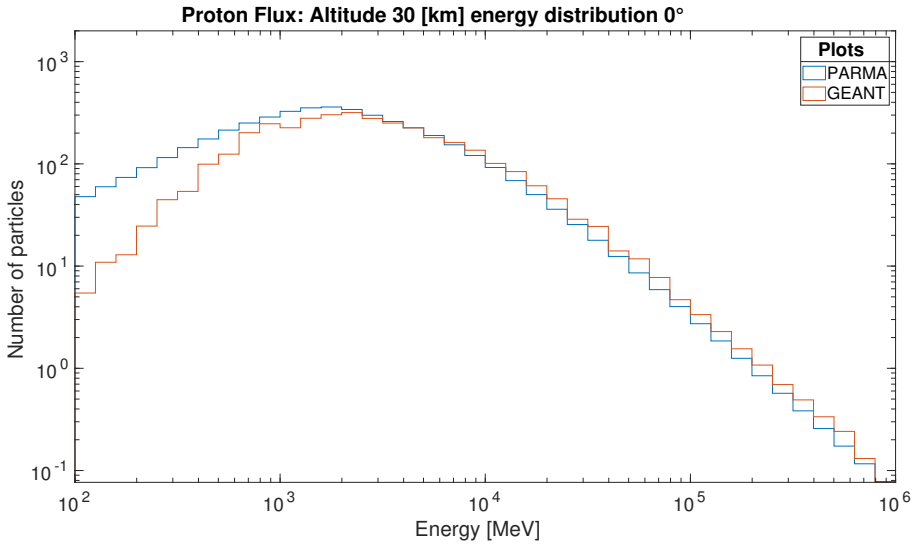

Figure 6.11: Energy spectra for PARMA and GEANT4 simulation at 30 km altitude above MSL and 0° zenith angle. The blue histogram corresponds to PARMA and the red histrogram to simulation results from GEANT4.

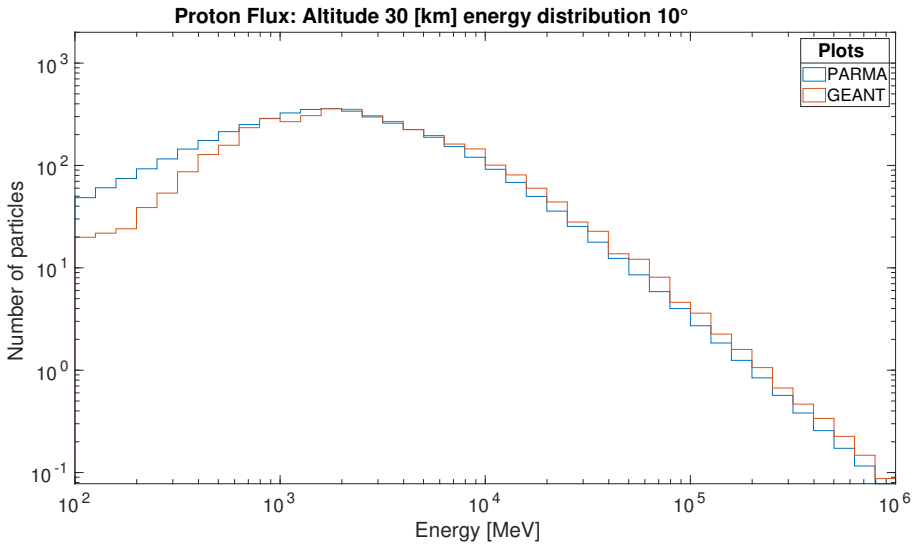

Figure 6.12: Energy spectra for PARMA and GEANT4 simulation at 30 km altitude above MSL and 10° zenith angle. The blue histogram corresponds to PARMA and the red histrogram to simulation results from GEANT4.

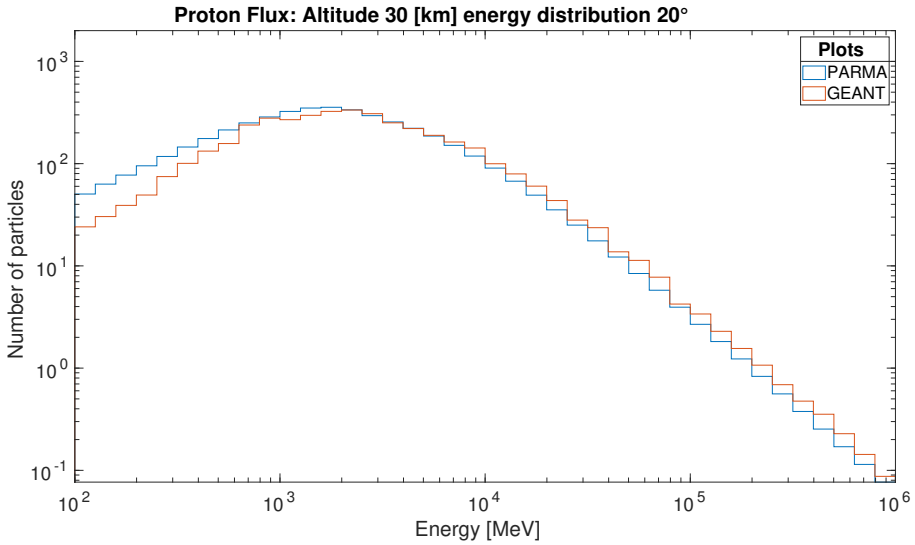

Figure 6.13: Energy spectra for PARMA and GEANT4 simulation at 30 km altitude above MSL and 20° zenith angle. The blue histogram corresponds to PARMA and the red histrogram to simulation results from GEANT4.

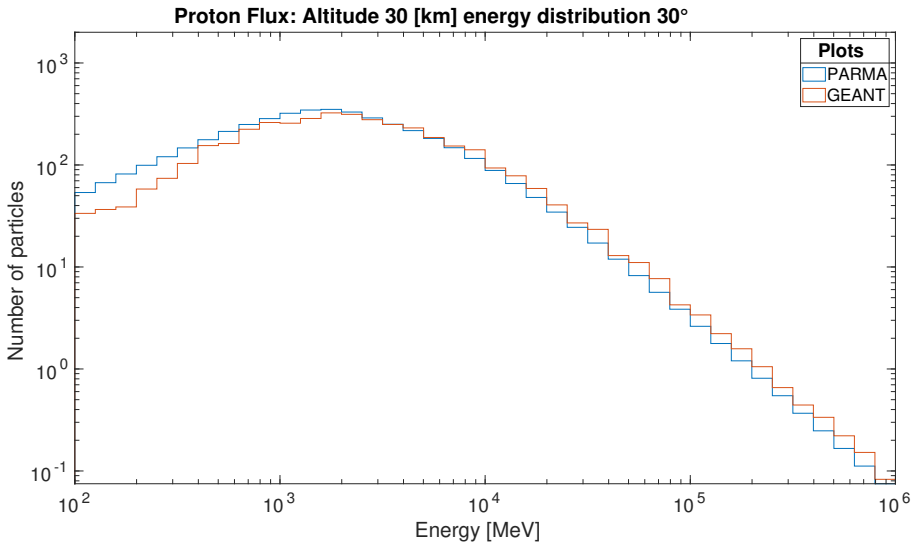

Figure 6.14: Energy spectra for PARMA and GEANT4 simulation at 30 km altitude above MSL and 30° zenith angle. The blue histogram corresponds to PARMA and the red histrogram to simulation results from GEANT4.

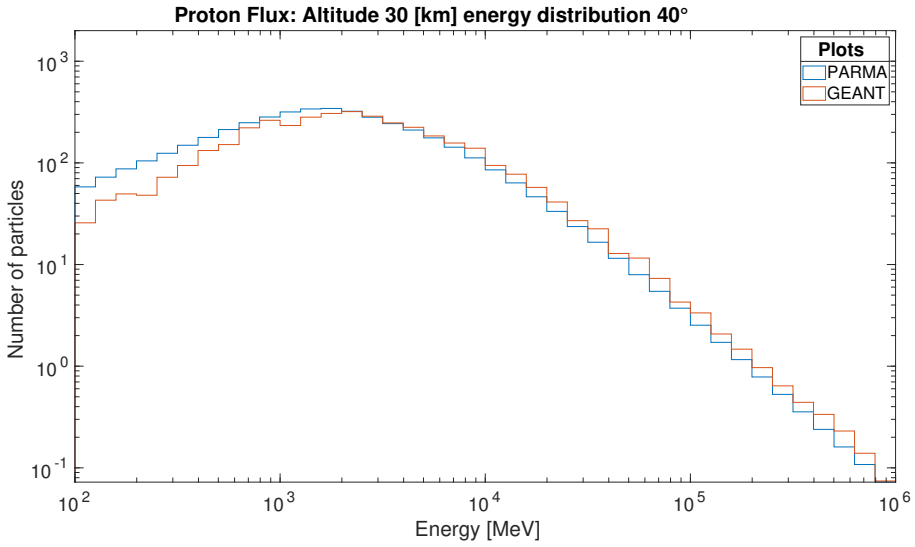

Figure 6.15: Energy spectra for PARMA and GEANT4 simulation at 30 km altitude above MSL and 40° zenith angle. The blue histogram corresponds to PARMA and the red histrogram to simulation results from GEANT4.

6.1.4 Comparison at 20 km

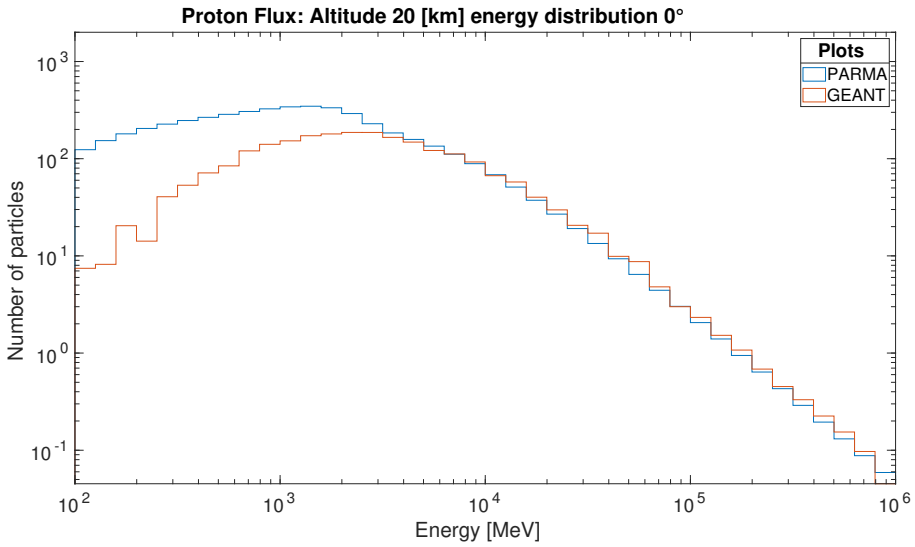

Figure 6.16: Energy spectra for PARMA and GEANT4 simulation at 20 km altitude above MSL and 0° zenith angle. The blue histogram corresponds to PARMA and the red histrogram to simulation results from GEANT4.

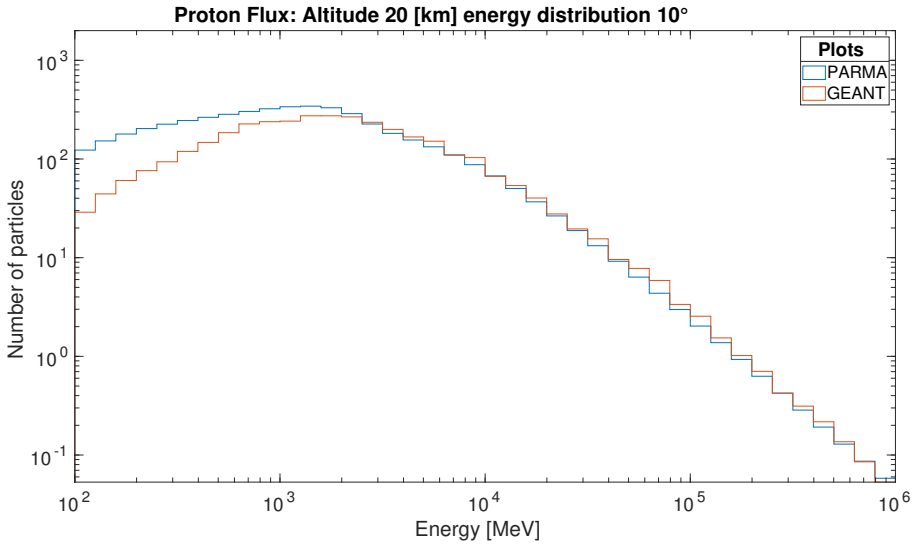

Figure 6.17: Energy spectra for PARMA and GEANT4 simulation at 20 km altitude above MSL and 10° zenith angle. The blue histogram corresponds to PARMA and the red histrogram to simulation results from GEANT4.

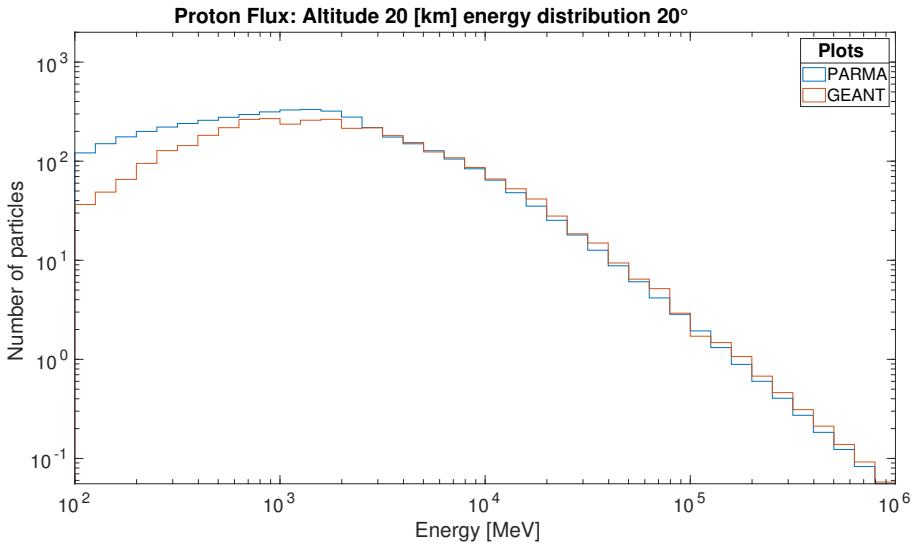

Figure 6.18: Energy spectra for PARMA and GEANT4 simulation at 20 km altitude above MSL and 20° zenith angle. The blue histogram corresponds to PARMA and the red histrogram to simulation results from GEANT4.

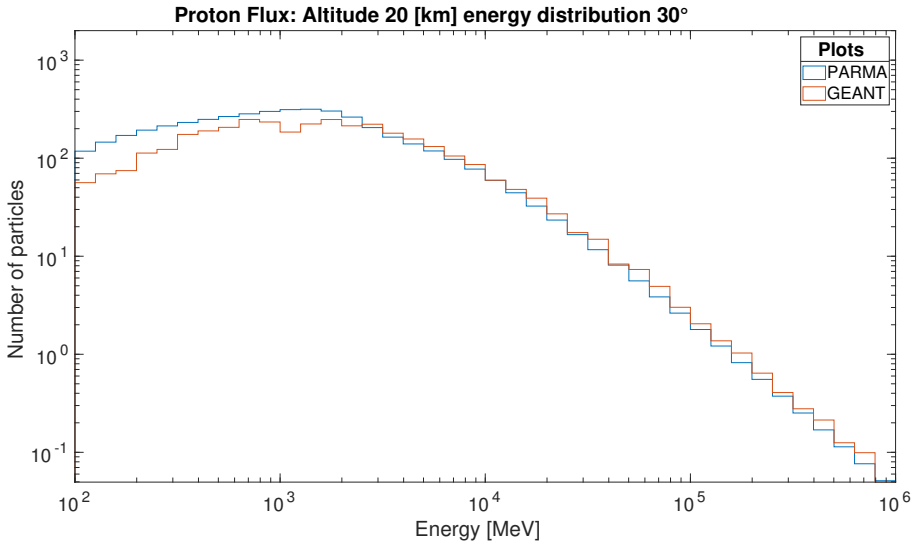

Figure 6.19: Energy spectra for PARMA and GEANT4 simulation at 20 km altitude above MSL and 30° zenith angle. The blue histogram corresponds to PARMA and the red histrogram to simulation results from GEANT4.

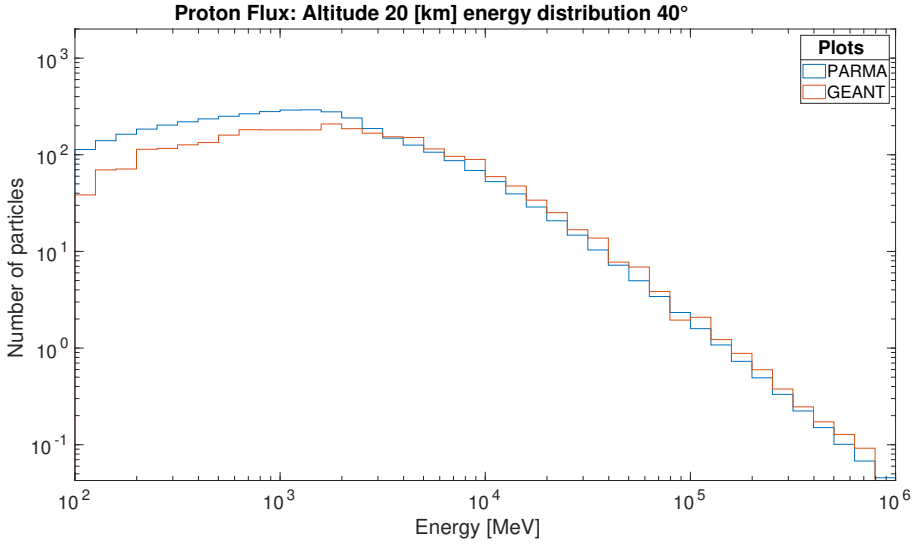

Figure 6.20: Energy spectra for PARMA and GEANT4 simulation at 20 km altitude above MSL and 40° zenith angle. The blue histogram corresponds to PARMA and the red histrogram to simulation results from GEANT4.

6.1.5 Comparison at 10 km

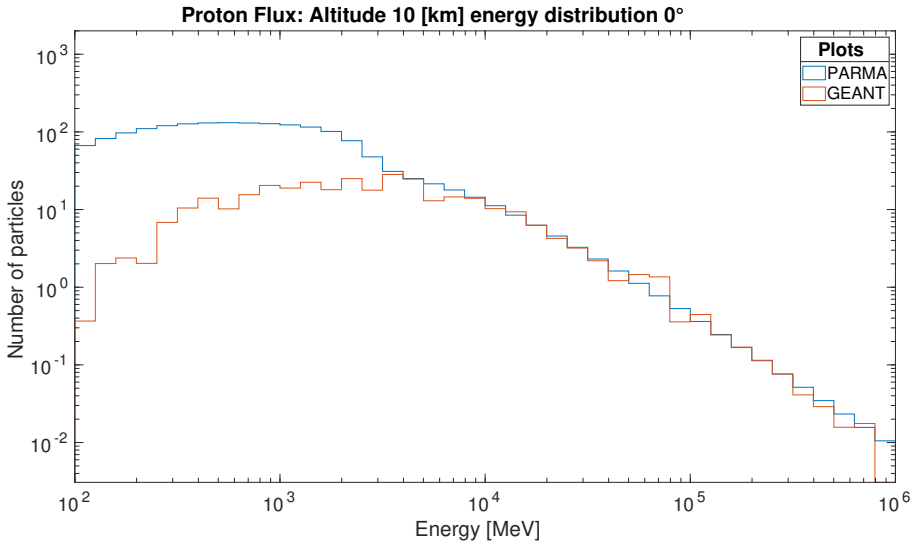

Figure 6.21: Energy spectra for PARMA and GEANT4 simulation at 10 km altitude above MSL and 0° zenith angle. The blue histogram corresponds to PARMA and the red histrogram to simulation results from GEANT4.

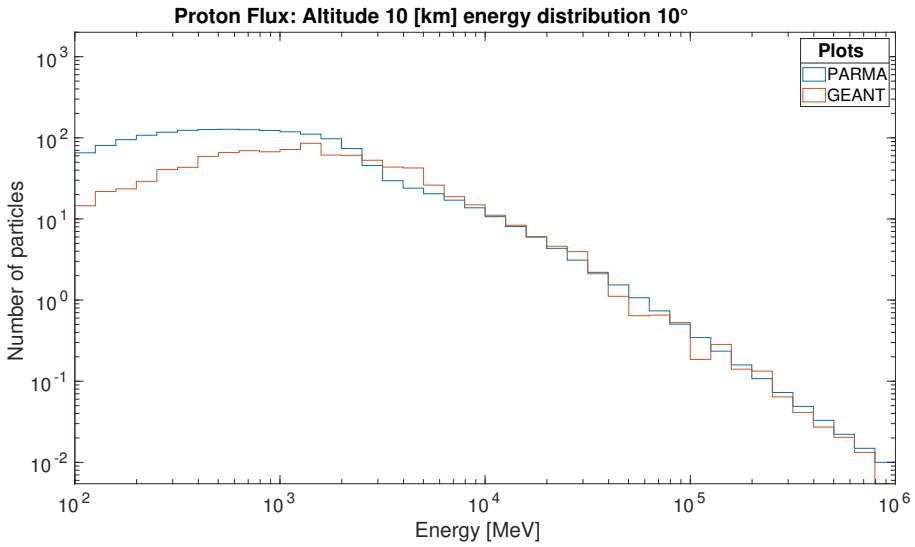

Figure 6.22: Energy spectra for PARMA and GEANT4 simulation at 10 km altitude above MSL and 10° zenith angle. The blue histogram corresponds to PARMA and the red histrogram to simulation results from GEANT4.

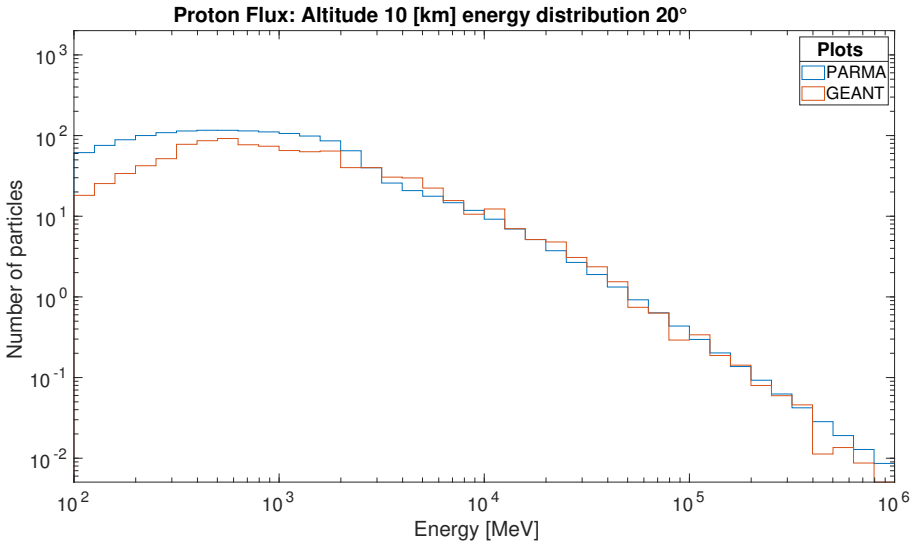

Figure 6.23: Energy spectra for PARMA and GEANT4 simulation at 10 km altitude above MSL and 20° zenith angle. The blue histogram corresponds to PARMA and the red histrogram to simulation results from GEANT4.

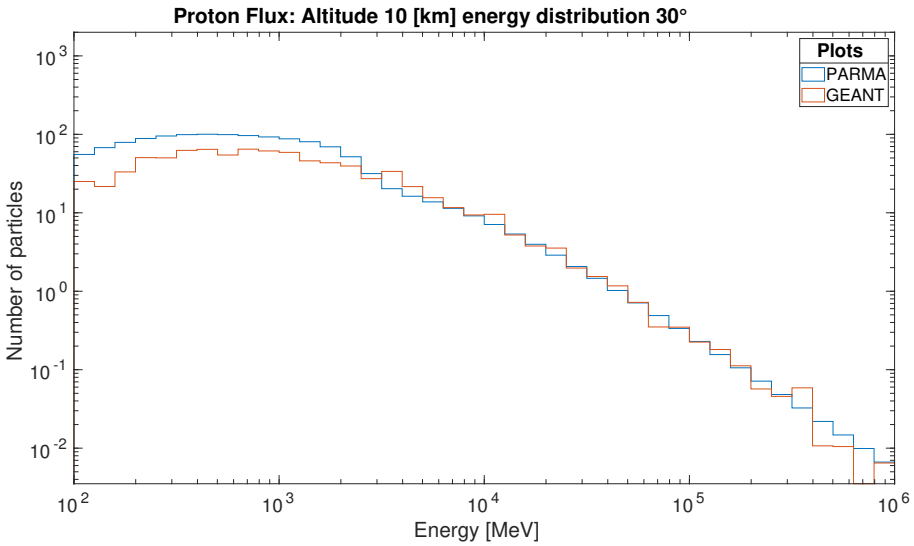

Figure 6.24: Energy spectra for PARMA and GEANT4 simulation at 10 km altitude above MSL and 30° zenith angle. The blue histogram corresponds to PARMA and the red histrogram to simulation results from GEANT4.

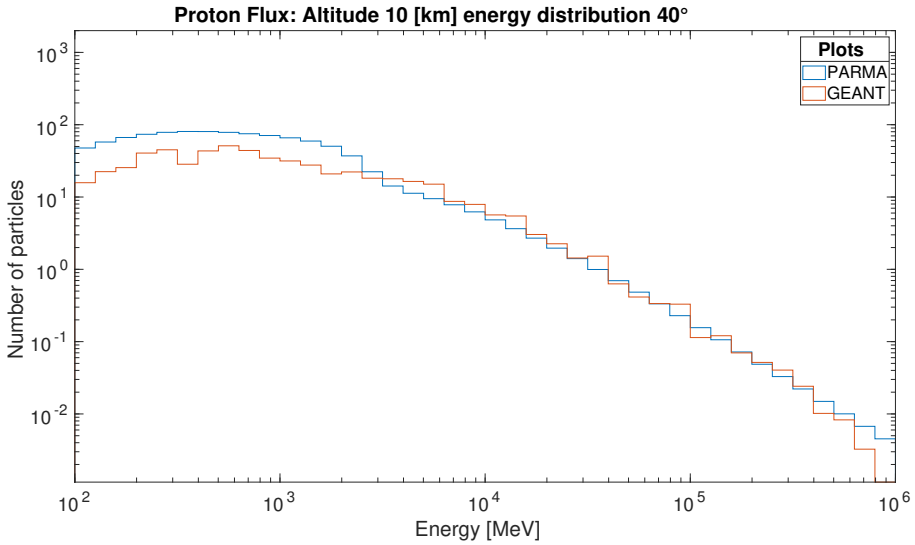

Figure 6.25: Energy spectra for PARMA and GEANT4 simulation at 10 km altitude above MSL and 40° zenith angle. The blue histogram corresponds to PARMA and the red histrogram to simulation results from GEANT4.

6.2 Discrepancies between PARMA and GEANT4

As we analyze the distributions at record altitude 40 km in Figure 6.6, Figure 6.7, Figure 6.8, Figure 6.9 and Figure 6.10 we see that the lower energies show a pattern of lower number of particle counts in the GEANT4 simulation results than the PARMA database. This is visible in the range of energies $10^2 - 3x10^2$ MeV.

The pattern of discrepancies for lower energies continues for the energy distributions for altitude 30 km in Figure 6.11, Figure 6.12, Figure 6.13, Figure 6.14 and Figure 6.15 where the energy range of discrepancies is extended up to about 10^3 MeV.

Further the energy distributions for 20 km in Figure 6.16, Figure 6.17, Figure 6.18, Figure 6.19 and Figure 6.20 shows a greater discrepancy for the 0° and 10° zenith angle distributions than the 30° and 40° zenith angle distributions. The discrepancies are generally located to the energy range $10^2 - 3x10^3$ MeV.

For the the 10 km above MSL distributions in Figure 6.21, Figure 6.22, Figure 6.23, Figure 6.24 and Figure 6.25 the pattern prevails and the discrepancies are larger for 0° and 10°energy distributions than for the distributions in the range 20° - 40°.

From the analysis of the energy distributions we can draw the conclusion that the discrepancy between GEANT4 and PARMA is located to energies below $3x10^3$ MeV and that the higher energies (above 10^4 MeV) are represented with satisfactory accuracy with regards to the resolution of the simulation.

Chapter 7

Discussion

This chapter contains a discussion of the results described in Chapter 6. The discrepancies between GEANT4 and PARMA will be discussed and possible reasons for the discrepancies in the results will be given a review.

7.1 Transport of protons

The discrepancies in reproduction of energy distributions for protons as described in Section 6.2 are mainly in lower energy ranges below 10^4 MeV. Some discrepancies can be due to the course resolution of our angular sampling of initial particle distribution zenith angles or due to the inherent limitations of a simulation that only accounts for parts of the full angular spectrum of the particle fluxes. Another open point is the modeled atmosphere as described in Subsection 5.1.1. The modeled atmosphere is based on a finer resolution than the EAS simulations conducted to create the PARMA database as described in Subsection 4.1. The atmosphere used in PHITS simulations were based on the US Standard Atmosphere 1976 with 28 layers between 86km and 0km altitude. The cosmic ray data as presented in the PARMA database has been corrected according to the MSISE atmosphere as used during our simulations, but there can still be discrepancies due to the different simulations setups used to create the distributions.

Another source of discrepancies that could explain the results is differing cross sections between the two codes used for simulations. Although this is not likely in the energy range $10^2 - 10^6$ MeV, a complete review of the cross sections for interactions between protons and air could help explain the discrepancies that were observed.

The simulation results yields that the method developed can not reproduce the energy distributions for protons for lower energies than $3x10^3$ MeV. However at energies between $10^4 - 10^6$ Mev the results show good agreement between GEANT4 simulations and the PARMA database. The GEANT4 simulation setup can therefore reproduce the distributions in the energy range $10^4 - 10^6$ Mev.

Chapter 8

Future Work

This chapter contains an outline for further work that must be conducted in order to create a simulation tool that can be used to study gamma-ray glow production mechanisms in GEANT4 using the PARMA data base as source for cosmic ray energy distributions. As shown in Chapter 7 the reproduction of particle distributions in GEANT4 is not a straight forward procedure and we therefore want to discuss what can be further done in order to complete the task and lay the ground for further development of the simulation tool.

8.1 Transport of protons

For further studies of the ability of GEANT4 to reproduce the proton energy distribution at energies between $10^2 - 3x10^3$ MeV the following steps should be taken.

The atmosphere resolutions should be checked. The simulations conducted to create the PARMA database described in Section 4.1 has a courser atmospheric resolution than the modeled atmosphere in GEANT4. Although the results in the PARMA database is interpolated and corrected to MSISE atmosphere for a given latitude the results can still be inaccurate compared to a finer modeled atmosphere. Therefore simulations should be conducted with the exact same resolution as described in Section 4.1.

The cross sections for interactions between protons and air in both the PHITS code described in Section 4.1 and GEANT4 should be compared in the energy range $10^2 - 10^6$ MeV for possible discrepancies in order to ensure that the two codes calculate interactions in the same manner.

8.2 Transportation of electrons, positrons and gamma-rays

For study of cosmic rays as seed particles for gamma-ray glow production it is necessary to study the distribution of these particles between altitudes above the thunderclouds we want to study, typically 20 km and down to the regions in the thundercloud where they can interact with the electrical fields and produce increases in the gamma-ray radiation.

The distributions from PARMA for electrons, positrons and gamma-rays must be compared with simulation results from GEANT4 as done with protons in Chapter 6.

8.3 Glow simulations

For simulation of gamma-ray glow production mechanisms using cosmic ray seed particles the observations from Chapter 3 has to be further analysed in order to set up simulation metrics that can be used in order to investigate how the thundercloud electrical fields in different regions of the thunderclouds together with the cosmic ray seed particles could explain the measurement values observed.

If the transport of electrons, positrons and gamma-ray particles from above thunderclouds can be modeled with satisfactory accuracy the GEANT4 simulations setup described in Subsection 5.2.2 can be utilized. In this setup electrical fields can be modeled between the charge regions of the thundercloud in order to simulate the large scale effects on charged cosmic ray particles from air showers in thunderstorm electrical fields. Also the flux at distances both vertical and horizontal to the production region could be analyzed to investigate the possible production of radiation at different locations than the measurement of the gamma-ray fluxes.

Chapter 9

Summary

The main objective of this thesis as been the development of a simulation tool for simulation of gamma-ray glows based on the modification of x-ray magnitude and energy spectra when using seed particles from the PARMA database.

For the verification of the feasibility of using the PARMA database as seed particles to our simulation we have simulated the propagation of protons from 50 km altitude to lower 10 km altitude. The assumption made is that the proton energy distributions are only affected by depositing energy to the atmosphere during propagation from higher to lower altitudes. Therefore we should be able to recreate the distributions if the two codes PHITS and GEANT4 calculates the propagation in the same manner.

The findings from our simulations show that the developed tool can simulate the energy distributions of protons with zenith angles 0° - 40° with good accuracy within the energy range $10^4 - 10^6$ MeV. For lower energies the results show a lower number of particles from the GEANT4 simulations than from the PARMA database.

The reproduction of electron, positron and gamma-ray distributions have not been completed and is therefore left for future work.

Bibliography

Buchvarova, M., H. Ruder, P. I. Velinov, and P. Tonev (2003), Ionization by galactic cosmic rays in the ionosphere and atmosphere depending on the solar activity, in *European Space Agency, (Special Publication) ESA SP*, 535. 2.2.1

CERN (), Geant4 Webpage. 4.2

Chilingarian, A., B. Mailyan, and L. Vanyan (2012), Recovering of the energy spectra of electrons and gamma rays coming from the thunderclouds, *Atmospheric Research*, *114-115*, doi:10.1016/j.atmosres.2012.05.008. (document), 2.13, 2.3.2

Chilingarian, A., G. Hovsepyan, and L. Vanyan (2014), On the origin of the particle fluxes from the thunderclouds: Energy spectra analysis, *EPL*, *106*(5), doi:10.1209/0295-5075/106/59001. (document), 1, 2.10, 2.3.2, 3.1

Dwyer, J. R. (2003), A fundamental limit on electric fields in air, *Geophysical Research Letters*, *30*(20), doi:10.1029/2003GL017781. (document), 1, 2.3.1, 2.3.1, 2.12, 3.2

Dwyer, J. R., D. M. Smith, and S. A. Cummer (2012), High-energy atmospheric physics: Terrestrial gamma-ray flashes and related phenomena, doi:10.1007/s11214-012-9894-0. (document), 1, 2.3.1, 2.12, 3.1

Eack, K. B., W. H. Beasley, W. D. Rust, T. C. Marshall, and M. Stolzenburg (1996a), Initial results from simultaneous observation of X rays and electric fields in a thunderstorm, *Journal of Geophysical Research Atmospheres*, *101*(23), doi:10.1029/96jd01705. (document), 1, 3.1, 3.2, 3.1, 3.1, 3.2, 5.3

Eack, K. B., W. H. Beasley, W. D. Rust, T. C. Marshall, and M. Stolzenburg (1996b), X-ray pulses observed above a mesoscal convective system, *GEOPHYSICAL RESEARCH LETTERS*, *23*. 1, 3, 3.1, 3.1, 3.2

Eack, K. B., D. M. Suszcynsky, W. H. Beasley, R. Roussel-Dupre, and E. Symbalisty (2000), Gamma-ray emissions observed in a thunderstorm anvil, *Geophysical Research Letters*, *27*(2), doi:10.1029/1999GL010849. 1, 3.1, 3.1, 3.2

Geant4 Collaboration (2017), GEANT4 Guide For Physics Lists. 5.1.3

Gurevich, A. V., and G. M. Milikh (1999), Generation of X-rays due to multiple runaway breakdown inside thunderclouds, *Physics Letters, Section A: General, Atomic and Solid State Physics*, *262*(6), doi:10.1016/S0375-9601(99)00695-7. 1, 3.1, 3.2

Gurevich, A. V., G. M. Milikh, and R. Roussel-Dupre (1992), Runaway electron mechanism of air breakdown and preconditioning during a thunderstorm, *Physics Letters A*, *165*(5-6), doi:10.1016/0375-9601(92)90348-P. (document), 2.3.1, 2.12

Kelley, N. A. (2014), Long Duration Gamma-Ray Emission From Thunderclouds, *Tech. rep.*, UNIVERSITY OF CALIFORNIA SANTA CRUZ, Santa Cruz. 1, 3.1

Kochkin, P., A. P. van Deursen, M. Marisaldi, A. Ursi, A. I. de Boer, M. Bardet, C. Allasia, J. F. Boissin, F. Flourens, and N. Østgaard (2017), In-flight observation of Gamma ray glows by ILDAS, *Journal of Geophysical Research: Atmospheres*, *122*(23), doi:10.1002/2017JD027405. 1, 3.1, 3.2

Krehbiel, P. (1986), The electrical structure of thunderstorms. In The Earth's Electrical Environment, *Washington, DC: National Academy Press*, pp. 90–113. 2.1

Matthiä, D., T. Berger, A. I. Mrigakshi, and G. Reitz (2013), A ready-to-use galactic cosmic ray model, *Advances in Space Research*, *51*(3), doi:10.1016/j.asr.2012.09.022. 4.1

McCarthy, M., and G. K. Parks (1985), Further observations of Xrays inside thunderstorms, *Geophysical Research Letters*, *12*(6), doi:10.1029/GL012i006p00393. (document), 1, 3.1, 3.1, 3.1, 3.1, 3.2

McCarthy, M. P., and G. K. Parks (1992), On the modulation of X ray fluxes in thunderstorms, *Journal of Geophysical Research*, *97*(D5), doi:10.1029/91JD03160. 3.1, 3.2

Mironova, I. A., K. L. Aplin, F. Arnold, G. A. Bazilevskaya, R. G. Harrison, A. A. Krivolutsky, K. A. Nicoll, E. V. Rozanov, E. Turunen, and I. G. Usoskin (2015), Energetic Particle Influence on the Earths Atmosphere, doi:10.1007/s11214-015-0185-4. 2.2.1

M.J.Berger, J.H.Hubbell, S.M.Seltzer, J.Chang, J.S.Coursey, R.Sukumar, D.S.Zucker, and K.Olsen (1998), XCOM: Photon Cross Sections Database. (document), 2.6

Moss, G. D., V. P. Pasko, N. Liu, and G. Veronis (2006), Monte Carlo model for analysis of thermal runaway electrons in streamer tips in transient luminous events and streamer zones of lightning leaders, *Journal of Geophysical Research: Space Physics*, *111*(2), doi:10.1029/2005JA011350. (document), 2.11, 2.3.1

Østgaard, N., H. J. Christian, J. E. Grove, D. Sarria, A. Mezentsev, P. Kochkin, N. Lehtinen, M. Quick, S. Al-Nussirat, E. Wulf, G. Genov, K. Ullaland, M. Marisaldi, S. Yang, and R. J. Blakeslee (2019), Gamma Ray Glow Observations at 20-km Altitude, *Journal of Geophysical Research: Atmospheres*, *124*(13), doi:10.1029/2019JD030312. 1, 3.1, 3.1

Parks, G. K., B. H. Mauk, R. Spiger, and J. Chin (1981), Xray enhancements detected during thunderstorm and lightning activities, *Geophysical Research Letters*, *8*(11), doi:10.1029/GL008i011p01176. 1, 3, 3.1, 3.1, 3.1

Rakov, V. A., and M. A. Uman (2003), Lightning: Physics and Effects - Vladimir A. Rakov, Martin A. Uman - Google Books. (document), 2.1, 2.1.1, 2.2, 2.3, 2.1.2, 2.4, 2.1.4

Sato, T. (2015), Analytical model for estimating terrestrial cosmic ray fluxes nearly anytime and anywhere in the world: Extension of PARMA/EXPACS, *PLoS ONE*, *10*(12), doi:10.1371/journal.pone.0144679. 4.1

Sato, T. (2016), Analytical model for estimating the zenith angle dependence of terrestrial cosmic ray fluxes, *PLoS ONE*, *11*(8), doi:10.1371/journal.pone.0160390. (document), 4.1, 4.1

Smart, D. F., and M. A. Shea (2005), A review of geomagnetic cutoff rigidities for earth-orbiting spacecraft, *Advances in Space Research*, *36*(10), doi:10.1016/j.asr.2004.09.015. 2.2.1

Stanev, T. (2010), Cosmic rays at the top of the atmosphere, in *High Energy Cosmic Rays*, doi:10.1007/978-3-540-85148-6{_}5. 2.2.1

Stolzenburg, M., W. D. Rust, and T. C. Marshall (1998), Electrical structure in thunderstorm convective regions 3. Synthesis, *Journal of Geophysical Research Atmospheres*, *103*(D12), doi:10.1029/97JD03545. 2.1.2

Wikimedia Foundation (2021), Cumulonimbus cloud. (document), 2.1

Wilson, C. T. R. (1925), The acceleration of β-particles in strong electric fields such as those of thunderclouds, *Proc. Cambridge Philos. Soc.* (document), 1, 2.3.1, 3